AN ABSTRACT OF THE THESIS OF

MARK JOHN ALGUARD (Name) for the DOCTOR OF PHILOSOPHY (Degree)

in PHYSICS (Major) presented on March 30, 1973 (Date)

Title: STARK INDUCED INTENSITY BEATS IN LYMAN-BETA AND LYMAN-ALPHA EMISSION FROM BEAM-FOIL FORMED HYDROGEN ATOMS

Abstract approved: Redacted for privacy

Dr. Charles W. Drake, Jr.

Observed intensity fluctuations in the emission of Stark-perturbed Ly-α and Ly-β radiation from beam-foil formed atomic hydrogen are compared with theoretical calculations to yield information on the relative cross sections for creation of a hydrogen atom into the various ℓ-levels for $n = 2$ and $n = 3$. It is found that the s-levels are preferentially populated (compared with a statistical distribution) by more than a factor of three at the beam energies which were observed. The theory of quantum beats is found to adequately describe the variation of the intensity pattern with field strength and field orientation. The effects of the fringing field, the Zeeman splittings, and the hyperfine interaction on the observed signal are also studied.

Stark Induced Intensity Beats in Lyman-Beta and Lyman-Alpha Emission from Beam-Foil Formed Hydrogen Atoms

by

Mark John Alguard

A THESIS

submitted to

Oregon State University

in partial fulfillment of
the requirements for the
degree of

Doctor of Philosophy

June 1973

APPROVED:

Redacted for privacy

Associate Professor of Physics

in charge of major

Redacted for privacy

Chairman of Department of Physics

Redacted for privacy

Dean of Graduate School

Date thesis is presented March 30, 1973.

Typed by Clover Redfern for Mark John Alguard

ACKNOWLEDGMENTS

It is a pleasure to acknowledge those who contributed to this work. My major professor, Chalres W. Drake, Jr., has provided assistance and encouragement throughout the project. Professors Charles E. Johnson and Clifford E. Fairchild have taken an active interest, and have assisted with some data taking. Professor Fairchild deserves special thanks for standing in as thesis advisor while Professor Drake was on leave, and, for proofreading this manuscript. The Research Corporation has provided financial support through a Cottrell Grant to Professor Drake. The O.S.U. Computer Center has awarded a computer grant without which the data analysis would not have been possible. The Nuclear Physics Group at the University of Oregon have generously loaned their accelerator facilities. Appreciation is also expressed for a National Defense Educational Act Fellowship awarded me by Oregon State University. Finally, I would like to thank my wife, Teri, for her moral support and clerical assistance.

TABLE OF CONTENTS

LIST OF FIGURES

LIST OF TABLES

STARK INDUCED INTENSITY BEATS IN LYMAN-BETA AND LYMAN-ALPHA EMISSION FROM BEAM-FOIL FORMED HYDROGEN ATOMS

1. INTRODUCTION

Hydrogen, the simplest of all atomic systems, has been the subject of extensive investigation, both experimentally and theoretically, for many years (1). Consequently, its well understood properties often serve as a probe for measurements involving more complicated systems. The process to be studied in the present experiment is the passage of high energy protons through a thin carbon foil (2). The interaction between the protons and the foil particles results in electron capture by some of the protons, thus forming atomic hydrogen in various excited states. Subsequent radiative decay, from those atoms formed in the $n = 2$ and $n = 3$ levels, is analyzed to yield information about the nature of the proton-foil interaction. This information is in the form of relative cross sections for formation of the atom into the various ℓ-levels for each principal quantum number.

At the present time there is no adequate theoretical description of the beam-foil interaction. The proton undergoes many interactions while passing through the foil; however the total time spent in the foil, approximately 10^{-14} seconds, is very short compared with lifetimes of the excited hydrogen atom. Therefore treatments based upon the

assumption of local thermodynamic equilibrium are not likely to explain the observed alignment of the emerging beam. On the other hand, formally correct calculations using multichannel scattering theory are not yet tractable, considering the complicated target.

Some qualitative features of the atomic creation process are known, however. It has been shown that excited atomic states created deep within the foil have a negligible chance of emerging (3). Consequently, the surface of the carbon foil should make the dominant contribution to excited state formation. Since this surface is typically contaminated by such things as pump oil, it would not be expected that the relative excitation cross sections would be sensitive to the particular foil used. On the other hand, experimental results show that the charge state distribution of an emerging beam does indeed depend upon the foil material itself (4).

The most extensive use of the beam-foil technique has been in the measurement of atomic lifetimes (2) in field free experiments. The advantage of this method, compared to the more conventional gas target method (5), is that the position, and hence the time, at which excitation occurs is well defined. A complication, however, is that because of the well localized excitation process, quantum beats occur in the observed intensity pattern. This effect can severely influence the accuracy of lifetime measurements (6). It is therefore particularly valuable to obtain an understanding of the nature of the coherence

effects that occur within the excited beam.

In Chapter 2, the theory of quantum beats (6, 7) is formulated in terms of an initial density matrix for the excited beam. The theory is found to be an accurate description of the observed phenomenon in the present experiment. The results are not only a verification of the theory, but also give information about the excitation process in the form of relative cross sections for excitation of the beam to various upper levels.

1.1. Previous Experiments

In the present experiment an external electric field is used to mix the field free eigenstates of the $n = 2$ or $n = 3$ levels of the hydrogen atom. The observed quantum beats in the coherent Ly-α or Ly-β decay of this system are the subject of investigation. A previous experiment on quantum beats in Ly-β emission (8) was done in zero external fields. Consequently, the relative cross sections for excitation could only be determined for the 3p-states. In the present work, the mixing introduced by the external field allows the determination of relative cross sections for different ℓ-levels.

Although Ly-β radiation has not previously been seriously investigated with the present technique, Stark-induced quantum beats have been studied in Ly-α emission in three earlier experiments (9, 10, 11).

In the first report of Stark beats in the decay of beam-foil excited atomic systems, Bickel (9) observed beats in Ly-α emission at an apparent frequency approximately twice the perturbed $s_{\frac{1}{2}}$-$p_{\frac{1}{2}}$ splitting. This "frequency doubling" effect was not found in subsequent investigations by Sellin et al. (10), and Andrä (11), and was later attributed to experimental error (10, 11). A second discrepancy arose pertaining to the relative populations of the $s_{\frac{1}{2}}$- and $p_{\frac{1}{2}}$-levels. Bickel's results (9), both for the quantum beats experiment and a separate mean-lifetime measurement, indicated preferential excitation of the 2s-level, whereas the investigations of Sellin et al. (10) and Andrä (11) indicated that the $p_{\frac{1}{2}}$-level was most heavily populated. In addition, Andrä concluded that his results indicated an alignment of the atoms perpendicular to the beam axis, and that the motional electric fields influenced the decay in a fundamentally different way than electrostatic fields of equivalent strength.

Both of these conclusions (regarding the beam alignment and the effects of motional fields) are in disagreement with the usual theory of quantum beats after beam-foil excitation (Chapter 2). Therefore, in the present experiment it was decided to subject the theory, as applied to the $n = 3$ levels, to additional tests. As discussed in Chapter 6, no significant departure from theory is encountered in the present work. As a final investigation, Ly-α emission was studied in two experimental runs. Again the theory is

adequate and the discrepancy reported by Andrä, between application of static and motional electric fields, is not observed. A final point is that the present results indicate preferential excitation to s-states, both for the $n = 2$ and $n = 3$ levels, in agreement with results obtained from mean-lifetime measurements (9, 12).

Stark induced intensity beats in radiative decay from the $n = 3$ level have been observed in two previous experiments (13, 14). Andrä (14) observed intensity beats in Ly-β emission at frequencies corresponding to the Stark perturbed $j = \frac{1}{2}$ splittings, and also the $j = \frac{3}{2}$ splittings. Owing to the apparent complexity of the intensity pattern, no information on relative populations was obtained. Similarly, Sellin (13) observed intensity beats of relatively small amplitude in Stark perturbed Balmer-α emission corresponding to the $s_{\frac{1}{2}}$-$p_{\frac{1}{2}}$ splitting. In neither experiment was a quantitative interpretation of the data attempted.

2. THEORY OF THE EXPERIMENT

2.1. The Beam-Foil Method

The beam-foil method of forming excited states of atomic systems provides the basis for the present experiment. In this method (2), an ionic species of the element of interest is accelerated to a selected energy and directed into a target region where the experiment is performed. As the name implies, a thin foil (typically carbon) is placed perpendicularly in the beam path. Because of the complex nature of the beam-foil interaction, the emerging beam will contain a great variety of ionic and atomic species in all possible excited states. Since the foil is thin (200-2000 Å), the particle velocities remain well determined and a time study of the emerging excited atoms can be performed by studying the emitted radiation as a function of the distance the atoms have traversed since leaving the foil. For instance, the mean lifetime of a state can be measured by determining the rate of decrease in intensity (of an emission line from that state) with distance from the foil. Since beam velocities from 10^7 to 10^9 cm/sec are possible, lifetimes in the range 10^{-10} to 10^{-7} sec can be measured by this method. In addition, any oscillations superimposed on the decay curve, with frequencies less than about 10 GHz, can be resolved with an appropriately narrow field of view of the detection system (see Section 2.2b).

2.2. Theory of Quantum Beats

a. Beats in Zero External Field

In the usual theory of atomic excitation (15), it is assumed that each eigenstate of the atomic system is excited incoherently. Consequently, each radiative component will decay exponentially in time. If the spectral resolution of the detection system allows the observation of two or more transitions simultaneously, then, neglecting cascade contributions, the observed decay curve will be a sum of exponential decays, i.e., the time dependent intensity of light, $I(t)$, is given by

$$I(t) \propto \sum_i a_i \gamma_i e^{-\gamma_i t} , \qquad (1)$$

where γ_i is the decay constant for the ith atomic eigenstate, and a_i represents the initial population of this state. The sum is over all observable transitions.

It was first pointed out by Macek (6, 7) that the assumption of incoherent excitation may fail in beam-foil experiments. This is plausable from the uncertainty principle alone, since the time the atom spends in the foil is small ($\sim 10^{-14}$ sec). Therefore, the excited atom must have an energy uncertainty of order $\Delta E \sim h/\Delta t$, or $\Delta\omega \sim 10^{14}$ sec^{-1}. Thus, coherence between different fine

structure levels certainly can, in principle, exist, and coherence between states of different principal quantum number may even be possible in some cases.

By considering the symmetry of the beam-foil interaction, and with some reasonable assumptions about the nature of the interaction, Macek (6) was able to derive an expression for the intensity of emitted radiation as a function of time, polarization, and direction of observation. The results of his calculation were that oscillating intensity components (at frequencies corresponding to the splittings between fine and hyperfine structure states within each excited level) would in general exist if the beam was aligned in magnetic substates, and if the polarizations of emitted radiation were not detected with equal sensitivity. For Lyman series radiation in hydrogenic species, the explicit expression, ignoring hyperfine structure, is (8)

$$I(t) = Ke^{-\gamma t}[(4+7g)\sigma_1+(5+2g)\sigma_0+(4-2g)(\sigma_0-\sigma_1)\cos \omega t] \qquad (2)$$

where γ is the decay constant for the p-states, ω is the fine structure splitting of the $p_{\frac{1}{2}}$- and $p_{\frac{3}{2}}$-levels, and g is the detection efficiency ratio for light polarized perpendicular to the beam as compared to light polarized along the beam. The relative cross section for excitation into a p-state with $|m_\ell| = 1$ is represented by σ_1, and σ_0 likewise corresponds to $m_\ell = 0$.

Several previous experiments (8, 16-20) have detected intensity fluctuations of this variety for field free atoms (consequently known as zero field beats), and it is now known that magnetic substate alignment is a general phenomenon in beam foil experiments.

If an external electric field is present, as in the present experiment, the derivation of an expression relating the temporal dependence of the intensity to the significant parameters of the excitation process will be considerably more difficult. Also, this expression will depend not only on the relative populations of m_ℓ substates, but also on the relative population of different orbital angular momentum states.

b. Quantum Beats in an Applied Field

An excited atomic system in an external electric field is most easily described using the phenomenological theory of radiation damping as formulated by Lamb[1] (21). In this theory, the interaction of the atom with the radiation field is phenomenologically accounted for by an effective Hamiltonian, H_{eff}, which contains, in addition to the usual atomic Hamiltonian and the applied perturbation, an anti-hermitian damping Hamiltonian, H_r. This damping Hamiltonian is evaluated by determining the decay rates of the various excited states

[1]Although the general validity of the Bethe-Lamb theory has been subject to some debate in recent years (22, 23), the theory does indeed adequately describe the hydrogen atom (24, 25).

in a field free situation $[(H_r)_{kk'} = -i\delta_{kk'}\gamma_k/2]$.

Diagonalization of the effective Hamiltonian then yields the complex energy eigenvalues and eigenvectors. If an initial state, $|\psi(0)>$, is known, then an expansion of this state in terms of the eigenvectors will give the wave function at any later time (assuming that the applied perturbation is constant). Since the eigenvectors are non-orthogonal, owing to the non-hermiticity of H_{eff}, the expansion must be done carefully. Let Latin letters denote an orthonormal basis set, and Greek letters denote the eigenvectors. In general the two representations will be connected by a similarity transformation, R, i.e.,

$$|\alpha> = \sum_k |k> R_{k\alpha}, \tag{3}$$

and

$$|k> = \sum_\alpha |\alpha> R^{-1}_{\alpha k}. \tag{4}$$

Suppose the initial state is known in terms of the basis representation, i.e.,

$$|\psi(0)> = \sum_k a_k |k>. \tag{5}$$

Then,

$$|\psi(t)> = \sum_{k,\ell,\alpha} a_k R_{\ell\alpha} R^{-1}_{\alpha k} e^{-i\omega_\alpha t} |\ell>, \tag{6}$$

where ω_a is the complex energy eigenvalue of the ath eigenstate.

In the experiment reported here, the intensity of radiation emitted in transitions from the state $|\psi(t)\rangle$ to a set of ground states, $|0\rangle$, is monitored as a function of time. In the dipole approximation, the intensity of emitted radiation of polarization x for a transition from a state $|m\rangle$ to a state $|n\rangle$ is (26)

$$I^x = \frac{4e^2\omega^4}{3c^3} |\langle n|x|m\rangle|^2 . \qquad (7)$$

If $|m\rangle$ represents a linear combination of atomic eigenstates, Equation (7) still holds if ω (the angular frequency of emitted radiation) does not vary significantly over the frequency range of the included transitions. For a hydrogen atom in an excited state with a specified principal quantum number this condition is well met. Therefore, for the present experiment, the intensity of radiation as a function of time is

$$I^x(t) \propto \sum_0 |\langle 0|x|\psi(t)\rangle|^2 . \qquad (8a)$$

Equation (8a) represents the light intensity emitted from a single atom. In general each atom emerging from the foil will have its own wave function. The generalization of Equation (8a) is

$$I^x(t) \propto \frac{1}{N} \sum_{0,n} |\langle 0|x|\psi^n(t)\rangle|^2 , \tag{8b}$$

where n labels the wave function of a particular atom and N is the number of atoms emerging from the foil.

Inclusion of the explicit time dependence derived in Equation (6) results in

$$I^x(t) \propto \sum_{\alpha,\beta} [R^\dagger M^x R]_{\beta\alpha} [R^{-1} \rho (R^{-1})^\dagger]_{\alpha\beta} e^{-i(\omega_\alpha - \omega_\beta)t} , \tag{9}$$

where ρ, the initial density matrix of the system, is defined by

$$\rho_{jk} = \frac{1}{N} \sum_n a_j^n (a_k^n)^* , \tag{10}$$

and, M^x, the monitoring operator (40) for dipole radiation polarized in the x-direction, is defined by

$$M^x_{jk} = \sum_0 \langle 0|x|j\rangle^* \langle 0|x|k\rangle . \tag{11}$$

It should be noted that since the excited state is described by a non-hermitean Hamiltonian, R is, in general, nonunitary ($R^\dagger \neq R^{-1}$).

Inspection of Equation (9) shows that beats at a frequency

corresponding to the energy separation of two eigenstates (α, β) will occur only if both eigenstates connect to a common ground state via the dipole operator, and if the system can initially be prepared in a linear combination of these eigenstates, i.e., both M and R must connect the two eigenvectors.

2.3. The Monitoring Operator

As defined in Equation (11), the monitoring operator, M^x, monitors the total photon flux of polarization x, emitted in all directions. A real detector, however, subtends only a limited solid angle, and it may also sample two polarizations simultaneously.

Suppose a detector, located on the y-axis and subtending a small solid angle, has major and minor optical axes along the x-and z directions, respectively. Then the total fluxes of photons with x- and z-polarizations are sampled in the ratio of the detection efficiencies for the two polarizations. Defining g as the efficiency for detection of light polarized along the major optical axis to the efficiency for light polarized along the minor axis, the total monitoring operation will be

$$M_x \propto M^z + gM^y . \tag{12}$$

Alternatively, if the detection system views along the y-axis with its major optical axis in the x- direction, then,

$$M_y \propto M^z + gM^x . \tag{13}$$

For the detection system used in the present experiment (a grating spectrometer), the major optical axis has been determined to lie in the direction of grating rulings, or along the slit orientation (8). The beam axis and the electric field axis have been arbitrarily chosen to define the z - and y - directions, respectively. Therefore, either M_x or M_y will be appropriate, depending upon whether observation is made perpendicular to, or along the field axis. The determination of the spectrometer polarization, g, is described in Appendix A.

Figure 1 shows a schematic diagram of a typical detection system used to measure intensity as a function of position along the beam axis. Because a finite interval along the beam axis is observed, the actual signal, S, incident on the detector will be

$$S(t) = \int_0^\infty I(t')f(t, t')dt' , \tag{14}$$

where $f(t, t')$ is the beam sampling function, or slit function, for the detection system. Figure 2 defines the measured slit function for the present work (see Appendix B).

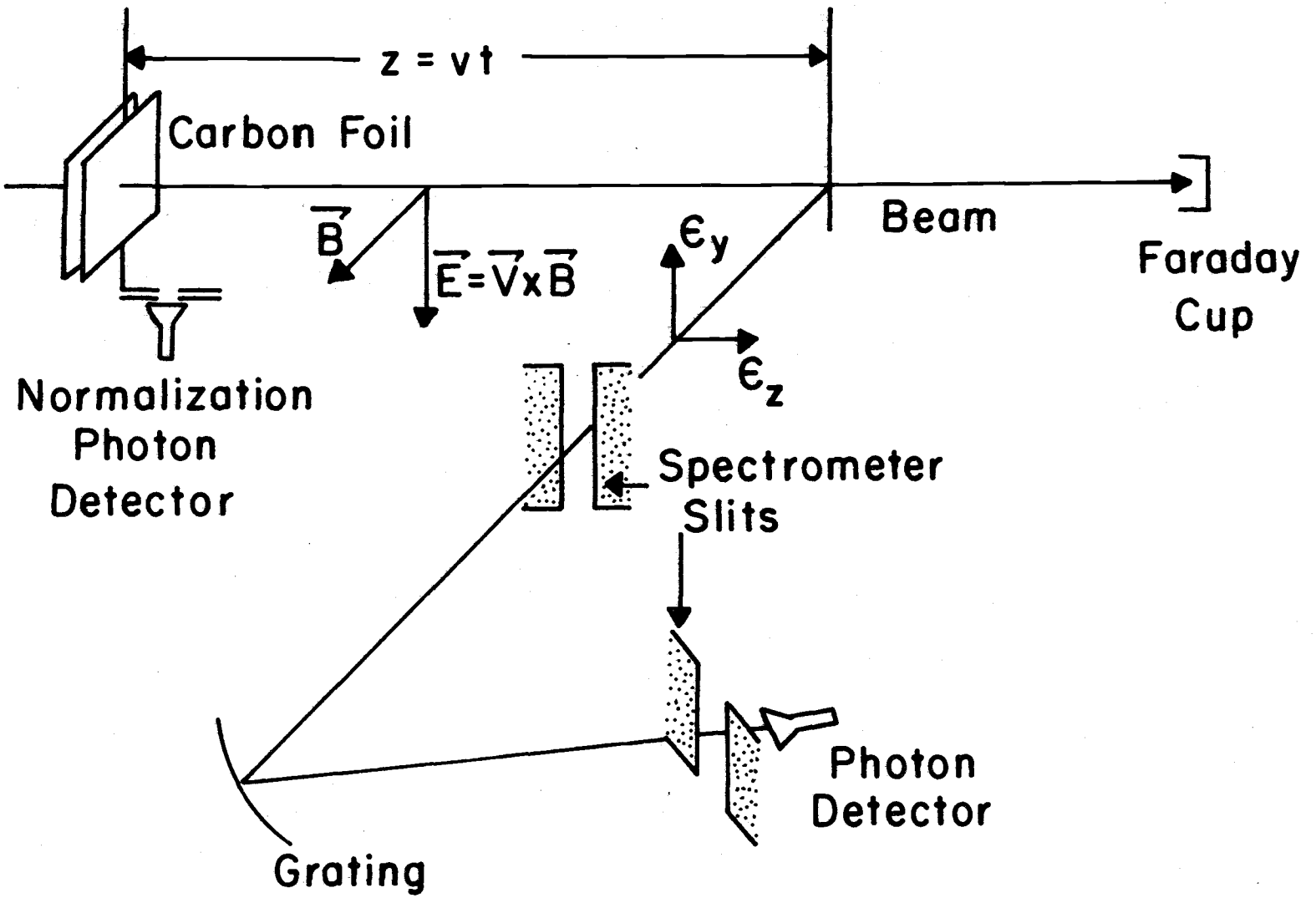

Figure 1. Schematic diagram of the detection system used to measure intensity of radiation of the beam as a function of the position along the beam axis.

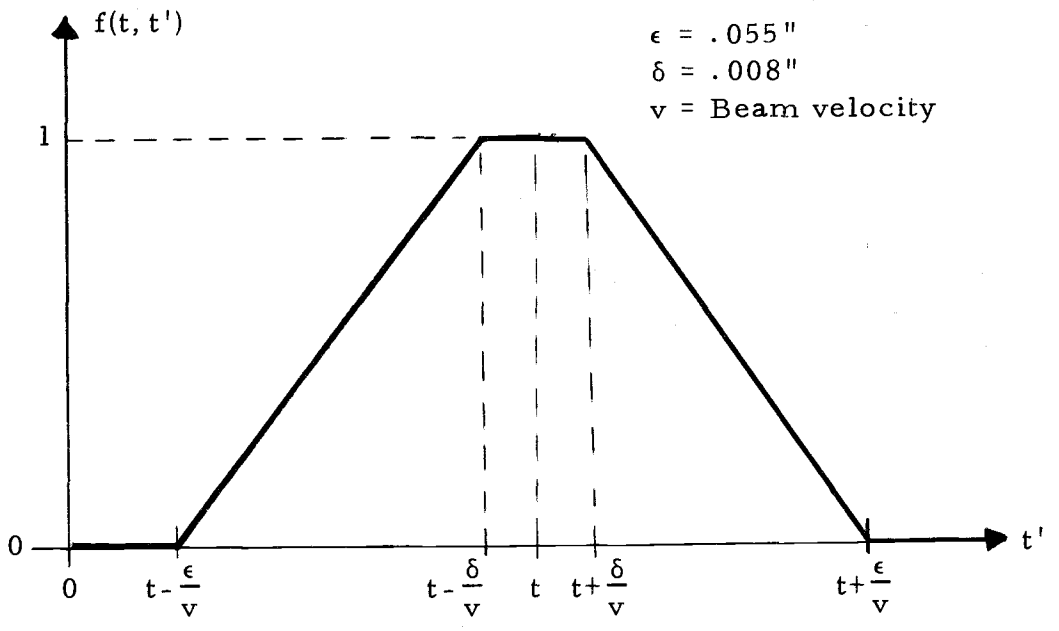

Figure 2. Shape of the measured slit function for the signal detection system.

Inserting Equation (9) into Equation (14) gives a complete expression for the observed signal,

$$S(t) = \sum_{a,\beta} b_{a\beta} [R^{\dagger} M R]_{\beta a} [R^{-1} \rho (R^{-1})^{\dagger}]_{a\beta} e^{-i(\omega_a - \omega_\beta^*)t} , \tag{15}$$

where

$$b_{a\beta} = \int_{-\infty}^{\infty} f(0, t') e^{-i(\omega_a - \omega_\beta^*)t'} dt' . \tag{16}$$

The integral in Equation (16) can easily be evaluated in closed form for the slit function defined in Figure 2. The result is

$$b_{a\beta} = \frac{2v^2}{(\epsilon - \delta)\omega_{a\beta}^2} \left[\frac{1}{\delta} \cos(\omega_{a\beta}\delta/v) - \frac{1}{\epsilon} \cos(\omega_{a\beta}\epsilon/v) + \frac{1}{\epsilon} - \frac{1}{\delta}\right]. \tag{17}$$

The objective of the present experiment is to determine the density matrix, ρ, of the atomic system. Equation (15), however, is still rather awkward for direct comparison with the observed signal. In general, for the $n = 3$ levels of hydrogen, the dimension of density matrix is 36 by 36 elements, and it is doubtful that all of these could be obtained from fitting Equation (15) directly to the data. Below it is shown that the symmetry of the beam-foil interaction severely restricts the form of the density matrix; it will be shown that only 10 independent elements remain.

2.4. The Density Matrix

The density matrix, ρ, which represents the state of the atomic system immediately after formation, was defined in Equation (10). The elements of this matrix represent the products of transition amplitudes for electron capture by the incident proton into the various atomic states, averaged over all incident particles:

$$\rho_{ij} = \langle a_i a_j^* \rangle, \tag{10'}$$

where a_i is the probability amplitude for creation of an atom in the state $|i\rangle$.

Macek (6) has shown that in general the phases between different states cannot be taken as random--except in that representation in which the collision Hamiltonian is diagonal. Using the terminology

of group theory, this means that ρ should commute with the entire symmetry group of the beam-foil interaction. Although the detailed interaction is unknown at this time (in fact, one purpose of the present experiment is to extract information concerning it), some rather general statements can be made about its symmetry (6).

If the foil is a random distribution of scattering centers, then the interaction Hamiltonian must have cylindrical symmetry about the beam axis. This means that ρ must commute with F_z the total angular momentum component along the beam direction. Therefore ρ is diagonal in the quantum number m_F. To a good approximation, electrostatic forces should dominate the interaction, with the result that ρ commutes with the entire rotation group for nuclear and electron spins. Consequently, ρ is not only diagonal in the quantum numbers m_I and m_s, but is independent of them. An additional symmetry is reflection in any plane containing the beam axis. This implies that ρ cannot depend upon the sign of the magnetic quantum number. Using the section rules just described, the most general form ρ can have is

$$\langle \ell', m'_\ell, m'_s, m'_I | \rho | \ell, m_\ell, m_s, m_I \rangle = \sigma(\ell, \ell', |m_\ell|) \delta_{m_\ell m'_\ell} \delta_{m_s m'_s} \delta_{m_I m'_I}, \tag{18}$$

where the quantization axis is taken to be along the beam direction. Therefore the density matrix, for $n = 3$ in hydrogen, depends, at

most, on the 10 parameters, $\sigma(\ell, \ell', |m_\ell|)$. In terms of these parameters, the density matrix can be rewritten as

$$\rho = \sum_{\ell, \ell', |m_\ell|} \sigma(\ell, \ell', |m_\ell|)\xi(\ell, \ell', |m_\ell|) , \tag{19}$$

where $\xi(\ell, \ell', |m_\ell|)$ is a matrix defined by

$$\xi(\ell, \ell', |m_\ell|) = \sum_{m_s, m_I, \text{ sign of } m_\ell} |\ell', m_\ell, m_s, m_I\rangle\langle \ell, m_\ell, m_s, m_I| . \tag{20}$$

Equation (15) can now be reformulated as

$$S_x(t) = \sum_{\ell, \ell', |m_\ell|} \sigma(\ell, \ell', |m_\ell|)\Omega_x(\ell, \ell', |m_\ell|; t) , \tag{21}$$

where

$$\Omega_x(\ell, \ell', |m_\ell|; t) = \sum_{\alpha, \beta} b_{\alpha\beta}[RM_xR^\dagger]_{\beta\alpha}[R^{-1}\xi(\ell, \ell', |m_\ell|)(R^{-1})^\dagger]_{\alpha\beta} \times e^{-i(\omega_\alpha - \omega_\beta^*)t} . \tag{22}$$

Equation (21) directly relates the experimental signal, $S(t)$, to the experimental unknowns, $\sigma(\ell, \ell', |m_\ell|)$.

The partial intensities, $\Omega_x(\ell, \ell', |m_\ell|; t)$, depend only upon the experimentally known monitoring operator, the applied

perturbation, and the slit function. Therefore, the partial intensities can first be calculated, and then a linear combination of them fitted to the measured intensity, $S(t)$. The fitting parameters will be the expansion coefficients, $\sigma(\ell, \ell', |m_\ell|)$, in Equation (19).

2.5. Calculations

a. Partial Intensities

In order to calculate the partial intensities, $\Omega(\ell, \ell', |m_\ell|; t)$, from Equation (22), the similarity transformation, R, must first be determined. It will be advantageous to neglect the effects of the hyperfine interaction and the Zeeman splittings for a first calculation. These effects will subsequently be considered as an additional perturbation. With this approximation, the effective Hamiltonian for a hydrogen atom with a specified principal quantum number, n in a constant electric field is

$$H_{eff} = H_0 + H_{fs} + H_s + H_r \ , \tag{23}$$

where H_s is the Stark perturbation, H_{fs} is the fine structure Hamiltonian, and H_r represents the interaction with the radiation field.

It will be advantageous to use the representation where H_{fs} and H_r are diagonal (the $|j\ell m_j>$ representation). The elements

of H_s for an electric field, $\vec{E}$, in the x - direction are given by

$$\langle j', \ell', m_j' | e\vec{E}\cdot\vec{r} | j, \ell, m_j \rangle = (-)^{\ell+j-\frac{1}{2}} \sqrt{\frac{(2\ell+1)(2j+i)}{2}}\, C(\ell, 1, \ell'; 0, 0, 0)$$

$$\times W(\ell, j, \ell', j'; \tfrac{1}{2}, 1)$$

$$\times \{C(jlj'; m_j, -1, m_j) - C(jlj'; m_j, 1, m_j')\}$$

$$\times \frac{3}{2} n \sqrt{n^2 - \ell_>^2}\, eE \,, \qquad (24)$$

where the C's and W's are Clebsh-Gordan and Racah coefficients, respectively, and $\ell_>$ is the greater of ℓ and ℓ'.

With this field orientation, the Stark perturbation can only mix levels with $\Delta\ell = \pm 1$ and $\Delta m_j = \pm 1$. Therefore H_s splits into two equivalent blocks according to whether $\ell + m_j + \frac{1}{2}$ is even or odd. Fortunately, the monitoring operator, M, also breaks up in this fashion and the first square bracket in Equation (22) vanishes if α and β correspond to different blocks. Consequently, initial coherence between opposite parity states can have no effect on the observed signal.

Listed below are the explicit forms of ρ, H_{eff} and M_y for that block of the $|j, \ell, m_j\rangle$ representation for which $\ell + m_j + \frac{1}{2}$ is even ($\sigma_{\ell|m_\ell|}$ denotes $\sigma(\ell, \ell, |m_\ell|)$, etc.):

$$
\rho = \begin{array}{c}
\begin{array}{cccccccccc}
\ell_j m_j: & s_{\frac{1}{2}}-\frac{1}{2} & p_{\frac{1}{2}}+\frac{1}{2} & p_{\frac{3}{2}}+\frac{1}{2} & p_{\frac{3}{2}}-\frac{3}{2} & d_{\frac{3}{2}}-\frac{1}{2} & d_{\frac{3}{2}}+\frac{3}{2} & d_{\frac{5}{2}}-\frac{1}{2} & d_{\frac{5}{2}}+\frac{3}{2} & d_{\frac{5}{2}}-\frac{5}{2}
\end{array} \\
\begin{pmatrix}
\sigma_s & 0 & 0 & 0 & \sigma_{sd} & 0 & \sigma'_{sd} & 0 & 0 \\
0 & \frac{\sigma_{p0}+2\sigma_{p1}}{3} & \frac{\sigma_{p1}-\sigma_{p0}}{\sqrt{9/2}} & 0 & 0 & 0 & 0 & 0 & 0 \\
0 & \frac{\sigma_{p1}-\sigma_{p0}}{\sqrt{9/2}} & \frac{2\sigma_{p0}+\sigma_{p1}}{3} & 0 & 0 & 0 & 0 & 0 & 0 \\
0 & 0 & 0 & \sigma_{p1} & 0 & 0 & 0 & 0 & 0 \\
\sigma_{sd} & 0 & 0 & 0 & \frac{2\sigma_{d0}+3\sigma_{d1}}{5} & 0 & \frac{\sigma_{d0}-\sigma_{d1}}{\sqrt{25/6}} & 0 & 0 \\
0 & 0 & 0 & 0 & 0 & \frac{\sigma_{d1}+4\sigma_{d2}}{5} & 0 & \frac{\sigma_{d2}-\sigma_{d1}}{5/2} & 0 \\
\sigma'_{sd} & 0 & 0 & 0 & \frac{\sigma_{d0}-\sigma_{d1}}{\sqrt{25/6}} & 0 & \frac{3\sigma_{d0}+2\sigma_{d1}}{5} & 0 & 0 \\
0 & 0 & 0 & 0 & 0 & \frac{\sigma_{d2}-\sigma_{d1}}{5/2} & 0 & \frac{4\sigma_{d1}+\sigma_{d2}}{5} & 0 \\
0 & 0 & 0 & 0 & 0 & 0 & 0 & 0 & \sigma_{d2}
\end{pmatrix}
\end{array} \tag{25}
$$

$$
H_{eff} = \begin{array}{c}
\begin{array}{ccccccccc}
s_{\frac{1}{2}}-\frac{1}{2} & p_{\frac{1}{2}}+\frac{1}{2} & p_{\frac{3}{2}}+\frac{1}{2} & p_{\frac{3}{2}}-\frac{3}{2} & d_{\frac{3}{2}}-\frac{1}{2} & d_{\frac{3}{2}}+\frac{3}{2} & d_{\frac{5}{2}}-\frac{1}{2} & d_{\frac{5}{2}}+\frac{3}{2} & d_{\frac{5}{2}}-\frac{5}{2}
\end{array} \\
\ell_j m_j : \\
\begin{pmatrix}
\nu_1 - \frac{i\gamma_s}{2} & -\sqrt{\frac{8}{9}}F & -\frac{2}{3}F & \sqrt{\frac{2}{3}}F & 0 & 0 & 0 & 0 & 0 \\
-\sqrt{\frac{8}{9}}F & -\frac{i\gamma_p}{2} & 0 & 0 & \sqrt{\frac{5}{18}}F & -\sqrt{\frac{5}{6}}F & 0 & 0 & 0 \\
-\frac{2}{3}F & 0 & \nu_2 - \frac{i\gamma_p}{2} & 0 & -\sqrt{\frac{4}{45}}F & -\sqrt{\frac{1}{15}}F & \sqrt{\frac{3}{10}}F & -\sqrt{\frac{3}{5}}F & 0 \\
\sqrt{\frac{4}{3}}F & 0 & 0 & \nu_2 - \frac{i\gamma_p}{2} & -\sqrt{\frac{1}{15}}F & 0 & -\sqrt{\frac{1}{10}}F & 0 & F \\
0 & \sqrt{\frac{5}{18}}F & -\sqrt{\frac{4}{45}}F & -\sqrt{\frac{1}{15}}F & \nu_3 - \frac{i\gamma_d}{2} & 0 & 0 & 0 & 0 \\
0 & -\sqrt{\frac{5}{6}}F & -\sqrt{\frac{1}{15}}F & 0 & 0 & \nu_3 - \frac{i\gamma_d}{2} & 0 & 0 & 0 \\
0 & 0 & \sqrt{\frac{3}{10}}F & -\sqrt{\frac{1}{10}}F & 0 & 0 & \nu_4 - \frac{i\gamma_d}{2} & 0 & 0 \\
0 & 0 & -\sqrt{\frac{3}{5}}F & 0 & 0 & 0 & 0 & \nu_4 - \frac{i\gamma_d}{2} & 0 \\
0 & 0 & 0 & F & 0 & 0 & 0 & 0 & \nu_4 - \frac{i\gamma_d}{2}
\end{pmatrix}
\end{array} \tag{26}
$$

$$M_y \propto \begin{array}{c} \begin{matrix} p_{\frac{1}{2}}+\frac{1}{2} & p_{\frac{3}{2}}+\frac{1}{2} & p_{\frac{3}{2}}-\frac{1}{2} \end{matrix} \\ \begin{pmatrix} \frac{1+g}{3} & \frac{1-2g}{\sqrt{18}} & \frac{1}{\sqrt{6}} \\ \frac{1-2g}{\sqrt{18}} & \frac{1+4g}{6} & \frac{1}{\sqrt{12}} \\ \frac{1}{\sqrt{6}} & \frac{6}{\sqrt{12}} & \frac{1}{2} \end{pmatrix} \end{array} . \qquad (27)$$

In Equation (26)

$$F = 5.75\ E(V/cm)\ MHz,$$

$$\nu_1 = 314.8\ MHz,$$

$$\nu_2 = 3250\ MHz,$$

$$\nu_3 = 3148.5\ MHz,$$

$$\nu_4 = 4333\ MHz,$$

$$\gamma_s = 1.0\ MHz,$$

$$\gamma_p = 29.5\ MHz,$$

and $$\gamma_d = 10.16\ MHz.$$

A computer routine (27) for diagonalizing non-hermitian matrices was used to compute the eigenvalues and eigenvectors (the similarity transformation, R) of H_{eff} at various values of the electric field. Figures 3 and 4 are plots of the calculated perturbed energies and decay rates for the various fine structure states of hydrogen with $n = 3$.

A second computer routine, developed by the present author, was used to calculate the partial intensities, $\Omega(\ell, \ell', |m_\ell|; t)$, from

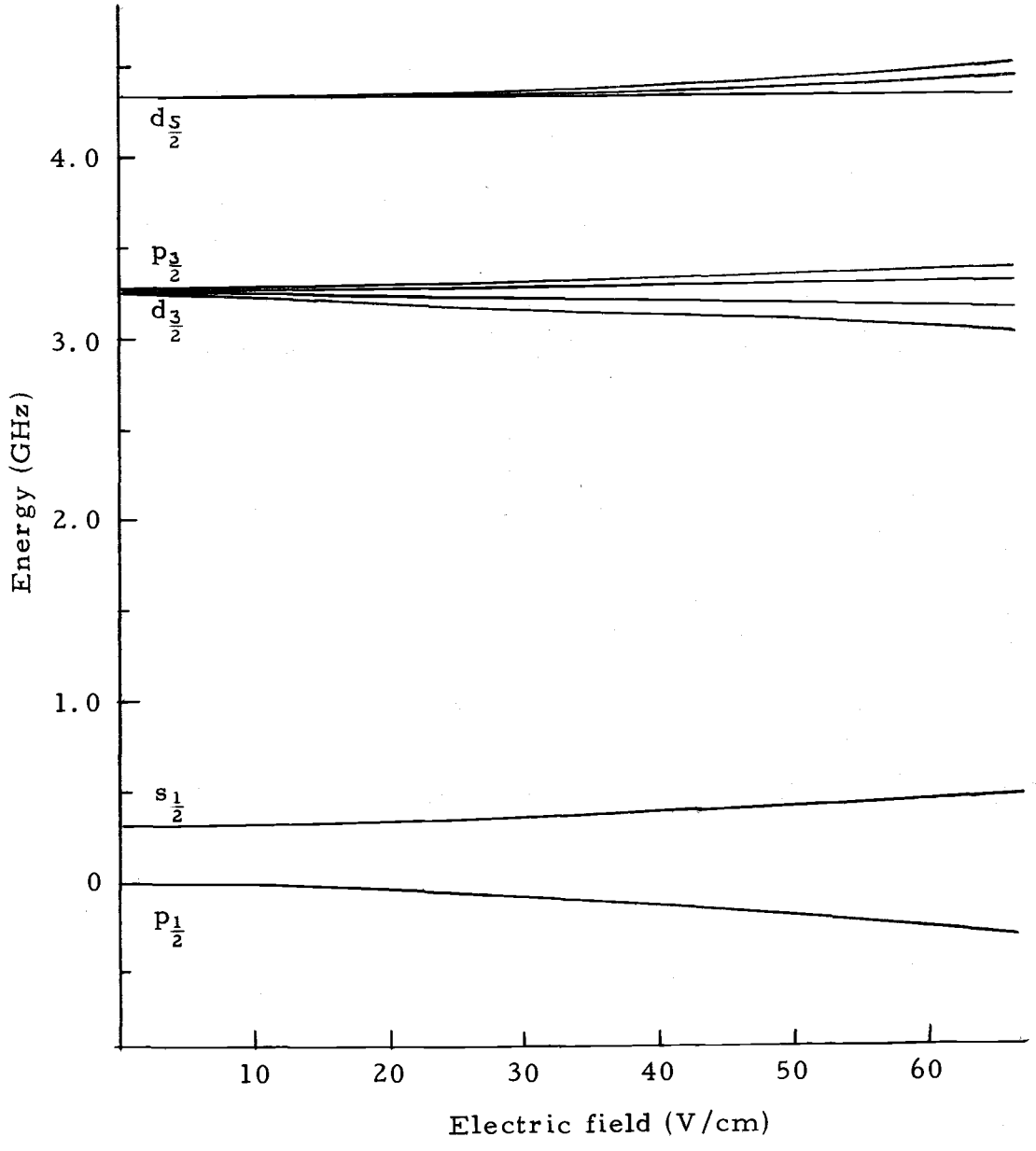

Figure 3. The Stark perturbed energy levels of the n = 3 states of hydrogen. The hyperfine interaction is not included.

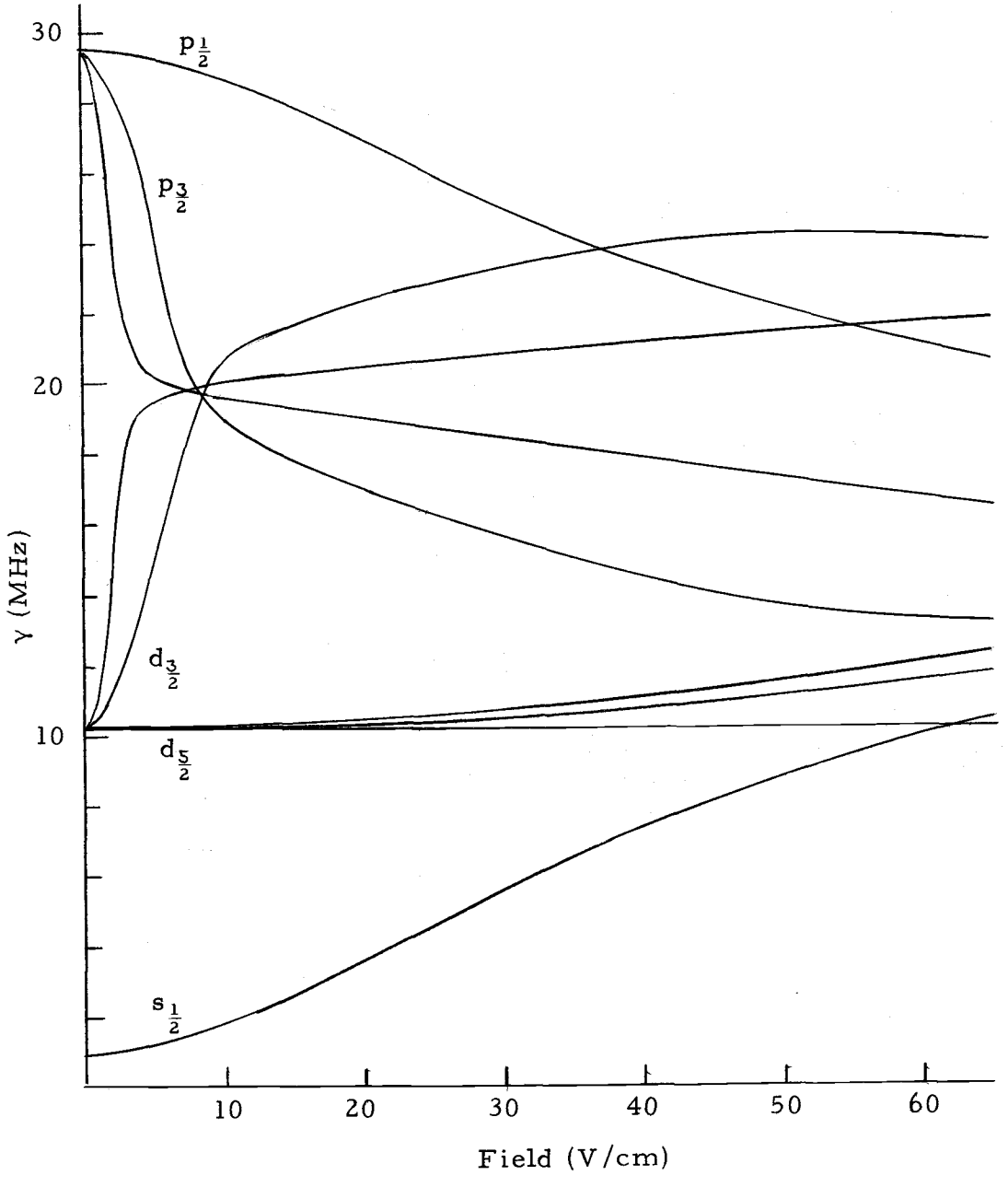

Figure 4. The Stark perturbed decay rates of the n = 3 states of hydrogen. The hyperfine interaction is not included.

Equation (22). Figure 5 shows the partial intensities calculated at a field strength of 53 V/cm for Ly-β emission.

Excluded from Figure 5 is the partial intensity corresponding to coherence between the s - and d-levels, $\Omega(s, d, 0; t)$. The contribution to the intensity pattern due to this term can be neglected in the present experiment for two reasons. First, since both the states are of even parity they contribute to Ly-β radiation only through coupling with the p-states via the applied electrostatic field. Therefore, the monitoring operator factor in Equation (22) will be small for those eigenstates with large s - and d - components. Furthermore, the applied perturbation mixes the s - and d-levels weakly, and the second bracket will be small except for the high frequency terms corresponding to the s-d beat frequency. The integrating factor, $b_{\alpha\beta}$, however makes this possibility unimportant since these high frequency beats are not normally resolved. In view of this reasoning, the large added difficulty (the coefficient $\sigma(s, d, 0)$ can be complex) of including the possibility of s-d coherence in the calculations did not appear to be justified.

Except for magnetic and hyperfine effects, and the possibility of coherence between the s - and d-states, an observed intensity pattern should be expressible as a linear combination of the six illustrated patterns. The relative proportions of the six patterns in the observed intensity will represent the relative cross sections for

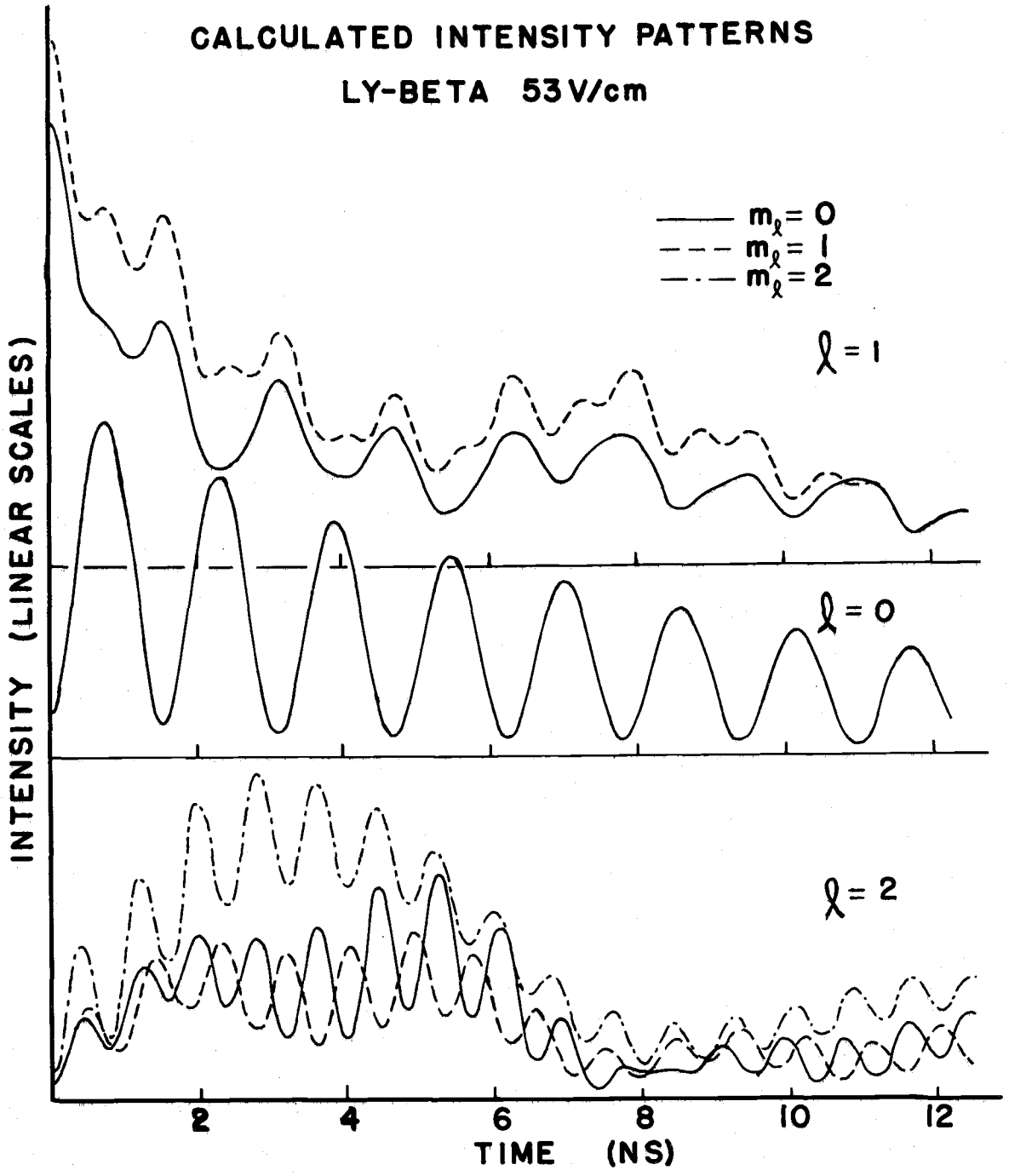

Figure 5. The calculated partial intensities for Ly-β emission in an applied electric field of 53 V/cm. The hyperfine and Zeeman interactions are not included in the calculation.

excitation of the atom into the six possible sets of states denoted by $\ell, |m_\ell|$.

The calculations show that the amplitude of the $s_{\frac{1}{2}}$-$p_{\frac{1}{2}}$ beat is essentially independent of the initial populations of the d-levels. (This is reasonable considering that the energy separation between the d-levels and the $j = \frac{1}{2}$ system is large compared with the magnitude of the perturbation.) The amplitude of the $s_{\frac{1}{2}}$-$p_{\frac{1}{2}}$ beat depends only upon the quantities σ_s, σ_{p1}, and σ_{p0}. If the ratio σ_{p1}/σ_{p0} is known, then the amplitude of this beat, relative to the initial intensity without the beat, depends only upon the ratio σ_s/σ_p, where $\sigma_p = \sigma_{p0} + 2\sigma_{p1}$ is the total cross section for excitation of p-states.

Using the previously measured (8, 16) ratio, $\sigma_{p1}/\sigma_{p0} = 1.4$ at 250 keV, the relative beat amplitudes depicted in Figure 6 were calculated. The indicated data points are measured beat amplitudes at this energy. This measurement is discussed in Section 4.3.

b. Hyperfine and Zeeman Effects

If the hyperfine and Zeeman interactions had been included in H_{eff}, above, the dimension of the matrix to be diagonalized would be increased from 9 by 9 to 36 by 36. In addition, the partial intensities themselves (Equation 22) would require a sum over 36^2 complex frequencies rather than the 9^2 resulting from neglecting these interactions. Since this must be done at each value of the time of interest,

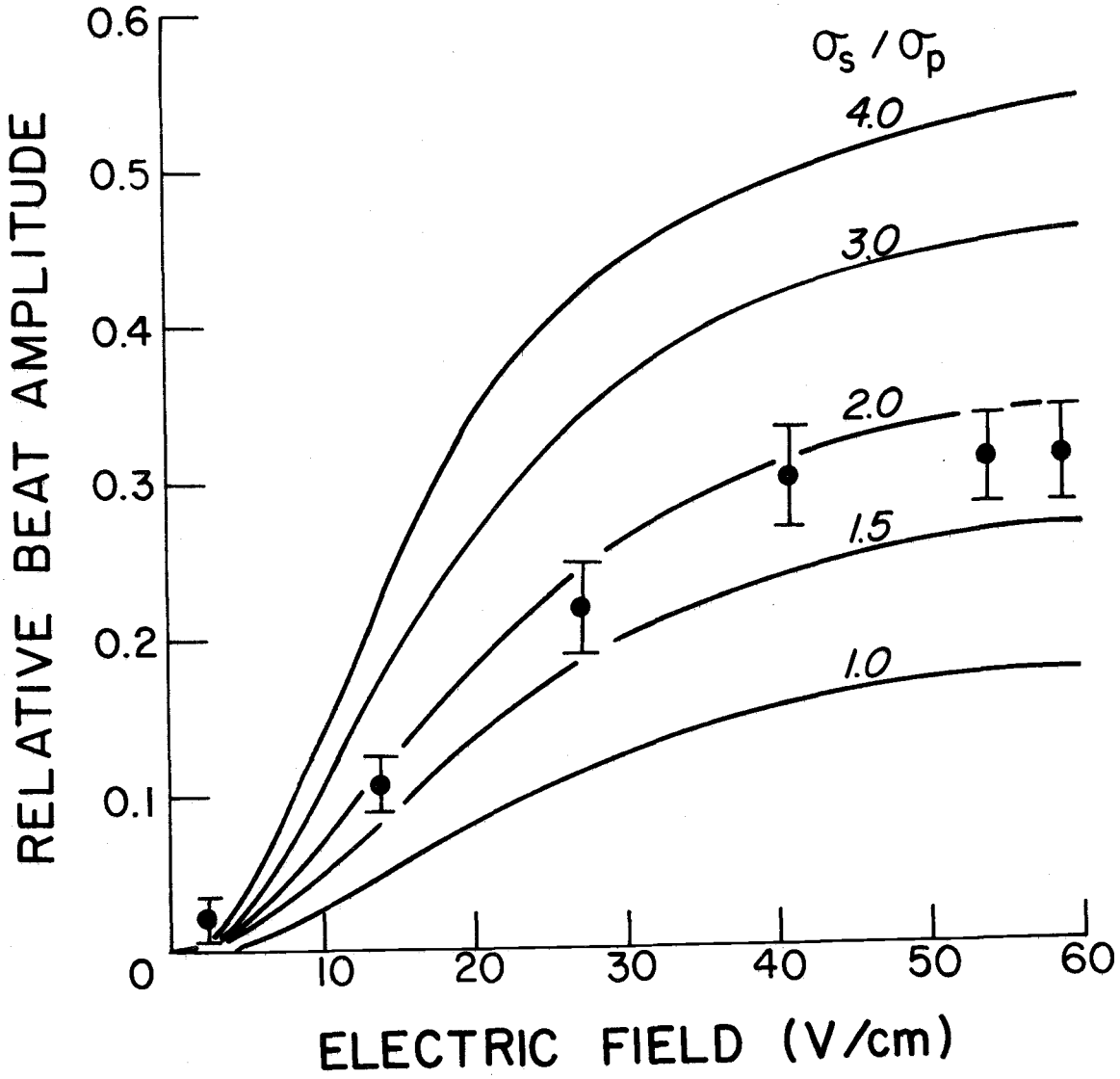

Figure 6. The amplitude of the n = 3 $s_{\frac{1}{2}}$-$p_{\frac{1}{2}}$ beat as a function of the applied electric field. The calculation assumes the ratio, $\sigma_{p1}/\sigma_{p0} = 1.4$, measured in a previous experiment (8).

considerably more computer time is required than for the more elementary calculation.

Although computing resources did not allow the complete calculation to be attempted, a considerable understanding of the effects which hyperfine and magnetic interactions have on the signal can be gained by considering a $j = \frac{1}{2}$ system (neglecting the $j = \frac{3}{2}$ and $j = \frac{5}{2}$ states). Such a system contains, in all, eight states, when the hyperfine interaction is included. The density matrix and monitoring operator for this system are

$$\langle \ell' F' m_F' | \rho | \ell F m_F \rangle = \delta_{\ell 1} \delta_{\ell \ell'} \delta_{FF'} \delta_{m_F m_F'} , \tag{28}$$

and

$$\langle \ell' F' m_F' | M | \ell F m_F \rangle = \delta_{\ell \ell'} \delta_{FF'} \delta_{m_F m_F'} . \tag{29}$$

Using the abbreviations

$\nu_1 = 328$ MHz,

$\nu_2 = 275$ MHz,

$\nu_3 = 5$ MHz,

$\nu_4 = -15$ MHz,

$\gamma_s = 1.0$ MHz,

$\gamma_p = 29.5$ MHz,

$g_s = 3.50$ MHz/gauss,

$g_p = 1.17$ MHz/gauss,

and $F = 5.75\, E(V/cm)$ MHz,

the effective Hamiltonian is

$$
H_{eff} = \begin{array}{c} {}^{F^{\ell}m_F}: \quad {}^{1}S_0 \quad {}^{0}S_0 \quad {}^{1}P_1 \quad {}^{1}P_{-1} \quad {}^{1}S_1 \quad {}^{1}S_{-1} \quad {}^{0}P_0 \quad {}^{1}P_0 \\ \left(\begin{array}{cccccccc} \nu_1 - \frac{i\gamma_s}{2} & 0 & -\frac{2}{3}F & \frac{2}{3}F & \frac{-iBg_s}{\sqrt{8}} & \frac{+iBg_s}{\sqrt{8}} & 0 & 0 \\ 0 & \nu_2 - \frac{i\gamma_s}{2} & \frac{2}{3}F & \frac{2}{3}F & \frac{-iBg_s}{\sqrt{8}} & \frac{-iBg_s}{\sqrt{8}} & 0 & 0 \\ -\frac{2}{3}F & \frac{2}{3}F & \nu_3 - \frac{i\gamma_p}{2} & 0 & 0 & 0 & \frac{-iBg_p}{\sqrt{8}} & \frac{-iBg_p}{\sqrt{8}} \\ \frac{2}{3}F & \frac{2}{3}F & 0 & \nu_3 - \frac{i\gamma_p}{2} & 0 & 0 & \frac{iBg_p}{\sqrt{8}} & \frac{iBg_p}{\sqrt{8}} \\ \frac{iBg_s}{\sqrt{8}} & \frac{iBg_s}{\sqrt{8}} & 0 & 0 & \nu_1 - \frac{i\gamma_p}{2} & 0 & \frac{2}{3}F & -\frac{2}{3}F \\ \frac{-iBg_s}{\sqrt{8}} & \frac{iBg_s}{\sqrt{8}} & 0 & 0 & 0 & \nu_1 - \frac{i\gamma_s}{2} & \frac{2}{3}F & \frac{2}{3}F \\ 0 & 0 & \frac{iBg_p}{\sqrt{8}} & \frac{iBg_p}{\sqrt{8}} & \frac{2}{3}F & \frac{2}{3}F & \nu_4 - \frac{i\gamma_p}{2} & 0 \\ 0 & 0 & \frac{iBg_p}{\sqrt{8}} & \frac{-iBg_p}{\sqrt{8}} & -\frac{2}{3}F & \frac{2}{3}F & 0 & \nu_3 - \frac{i\gamma_p}{2} \end{array} \right) \end{array} \quad (30)
$$

As in the fine structure calculation outlined above, the two partial intensities (corresponding to σ_s and σ_p) are calculated by first diagonalizing H_{eff} at the selected field strengths and then applying Equation (22). The dashed curve in Figure 7a is the result of a linear combination of the two patterns in the ratio $2{:}1 = \sigma_p : \sigma_s$. The field strengths are 50 V/cm and 10 gauss.

To consider what effect the hyperfine and Zeeman splittings have on the intensity, the calculation can be repeated neglecting these effects. The problem then simplifies to a two level system and can, in fact, be solved in closed form (28, 29). If this solution is superimposed on the previous calculation with the same choice of relative cross sections, $\sigma_s : \sigma_p = 2{:}1$, it is found that the two solutions agree well at zero time, but that the calculated beat decays much more rapidly in the first case. If, instead, the relative cross sections are adjusted, in the two level approximation, so as to obtain a best fit, the results shown in Figure 7a are obtained. The "measured" cross section ratio for these artificial data is $\sigma_s/\sigma_p = 1.75$ --an error of 0.25.

Obviously, the major effect of the hyperfine and Zeeman interactions over the time scale illustrated is to partially wash out the composite $s_{\frac{1}{2}}$-$p_{\frac{1}{2}}$ beat amplitude due to the several frequencies involved between these two levels getting progressively more out of phase as time increases. Since the beats all start in phase at $t = 0$,

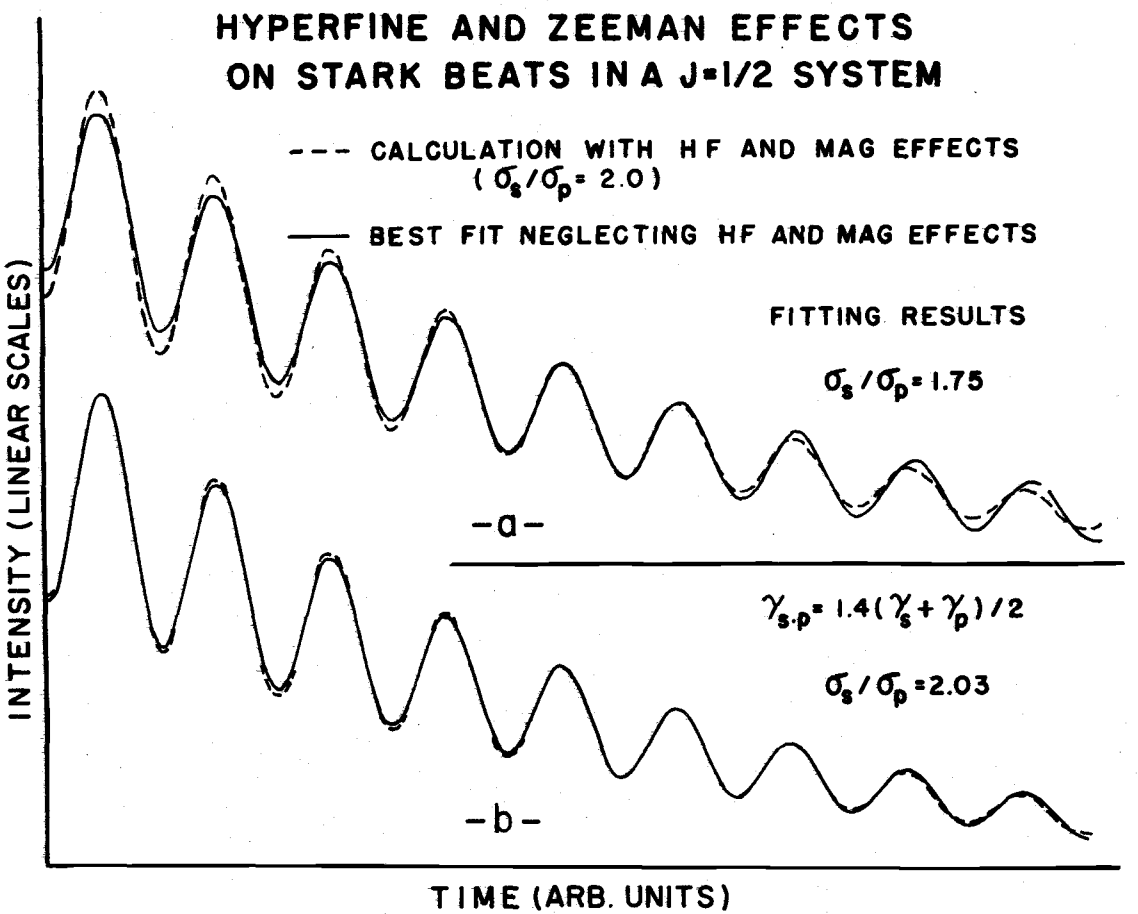

Figure 7. Hyperfine and Zeeman effects in a $j = \frac{1}{2}$ system with $\sigma_s/\sigma_p = 2.0$.

a) A best fit of the approximation neglecting hyperfine and Zeeman effects to the complete calculation yields $\sigma_s/\sigma_p = 1.75$.

b) A best fit if the decay rate of the $s_{\frac{1}{2}}$-$p_{\frac{1}{2}}$ beat is allowed to vary. The ratio, σ_s/σ_p, is determined to be 2.03, in good agreement with the assumed value.

the initial amplitudes calculated by the two methods agree. However, an attempt to fit to a mean amplitude results in an erroneous determination of σ_s/σ_p, since this ratio is determined by the initial amplitude.

Figure 7b results if the decay rate of the $s_{\frac{1}{2}}$-$p_{\frac{1}{2}}$ beat is adjusted to agree, as nearly as possible, with the eight-state result. This ad-hoc adjustment allows a better fit and a "measured" cross section ratio ($\sigma_s/\sigma_p = 2.03$) in good agreement with the actual value. Since this procedure results in an accurate determination of σ_s/σ_p, which is the purpose of this experiment, the same recipe is used when the $j = \frac{3}{2}$ and $\frac{5}{2}$ states are included; i.e., the $s_{\frac{1}{2}}$-$p_{\frac{1}{2}}$ beat decay rate is adjusted to best fit the observed data when an analysis is attempted. Beats at a frequency corresponding to the hyperfine splittings themselves are also present. Since only a fraction of a period of these frequencies are observed, their effect is small in the present experiment.

c. Fringing Fields

It is to be stressed that the above development and calculations are valid only if the perturbation is constant in time, i.e., if the electric field is uniform over the region where the beam is observed. This holds true for a motional electric field since the target holder is made of non-magnetic material and will not perturb the external field,

which is supplied by large coils external to the target region. However, for some data scans an electric field provided by condenser plates, as illustrated in Figure 8, was the source of the perturbation.

In general, the equation of motion of the time dependent density matrix is

$$\dot{\rho}(t) = -i[H(t)\rho(t) - \rho(t)H^{\dagger}(t)] , \tag{31}$$

where the Hamiltonian, H, may be an explicit function of time. In this formalism, the intensity of emitted radiation is

$$I(t) = Tr(M\rho(t)) . \tag{32}$$

For a constant perturbation this equation reduces to Equation (9), since, in this case

$$\rho(t) = e^{-iHt}\rho(0)e^{iH^{\dagger}t} . \tag{33}$$

It is to be stressed that the initial density matrix, $\rho(0)$, is the time independent density matrix discussed in the preceding sections. In Equation (15), for example, the time dependence is explicitly contained in the exponential factor. For a time dependent perturbation it will be necessary to integrate Equation (31) directly.

By the method of conformal mapping, the electrostatic potential, $\Phi(y, z)$, for the geometry illustrated in Figure 8 can be solved in closed form (with the simplifying assumption that the gaps between

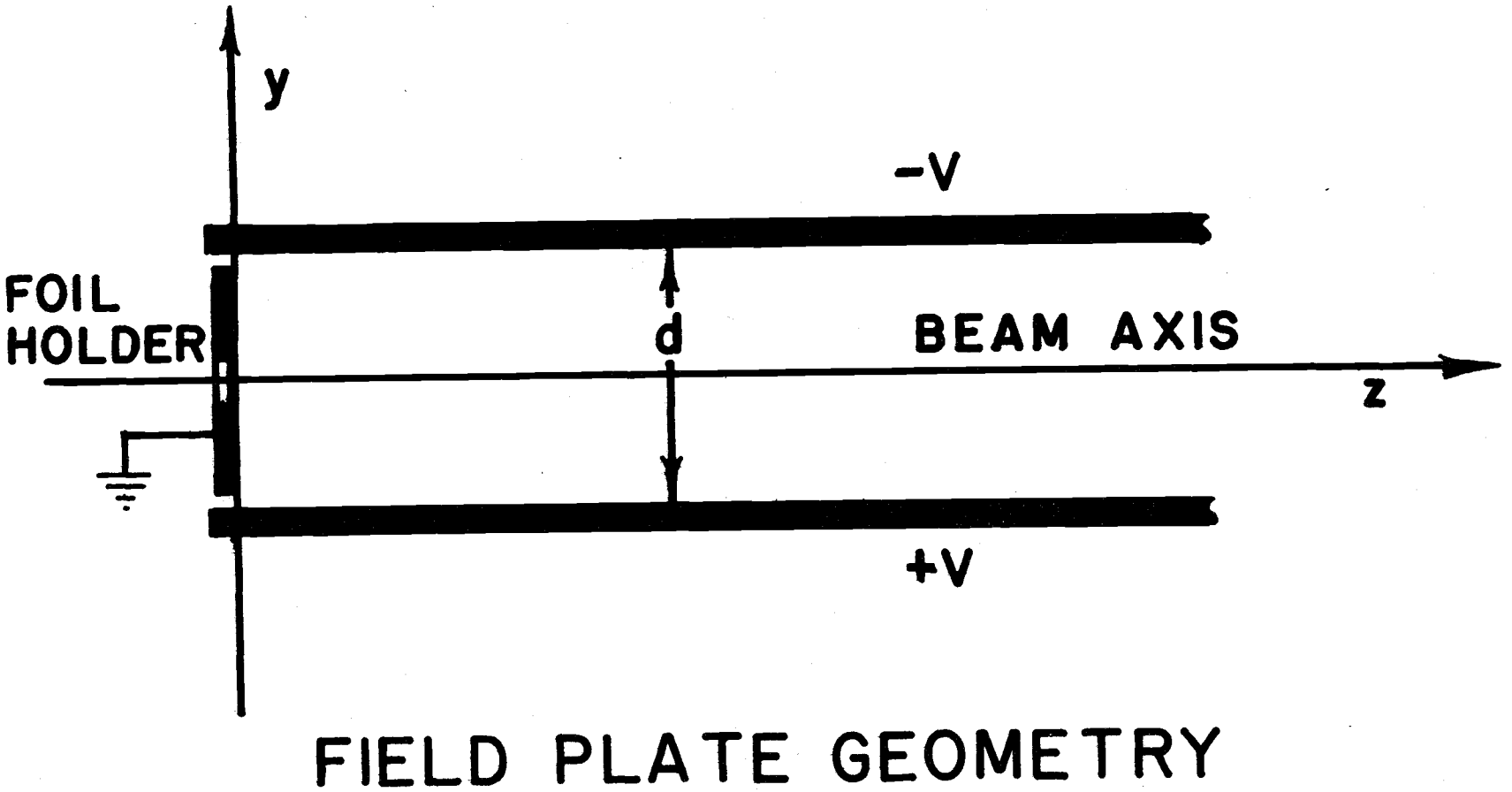

Figure 8. The electric field plates used to check the equivalence of static and motional electric fields. The plate separation is 1.27 cm.

target holder and field plates are small compared with the separation of the field plates). The result is

$$\Phi(y, z) = \frac{2V}{\pi}[\tan^{-1}(\frac{r+c}{s}) - \tan^{-1}(\frac{1+c}{s})] , \qquad (34)$$

where $r = e^{-2\pi z/d}$, $c = \cos(2\pi y/d)$, and $s = \sin(2\pi y/d)$. Differentiating, one gets the electric field components,

$$E_y = \frac{2V}{d}(1+r^2)/D , \qquad (35a)$$

and

$$E_z = -\frac{4V}{d} rs/D , \qquad (35b)$$

where $D = 1 + 2rc + r^2$.

Both parallel and perpendicular fields are, in general, present in the field region. The Hamiltonian will therefore mix all elements of the density matrix. A computer routine was written to integrate Equation (31) for the case where an atom enters the field at $z = 0$ with y held constant and a uniform velocity in the z-direction. The states included in the calculation are the $j = \frac{1}{2}$ system, neglecting hyperfine structure.

Figure 9a shows the results of this calculation if $y = 0$, and if the applied perturbation has a strength of 0.6 times the unperturbed $s_{\frac{1}{2}}$-$p_{\frac{1}{2}}$ splitting. The magnitude of the effect is best parameterized by the quantity $\alpha = \frac{\lambda_0}{\pi d}$ where λ_0 is the beat wavelength of the

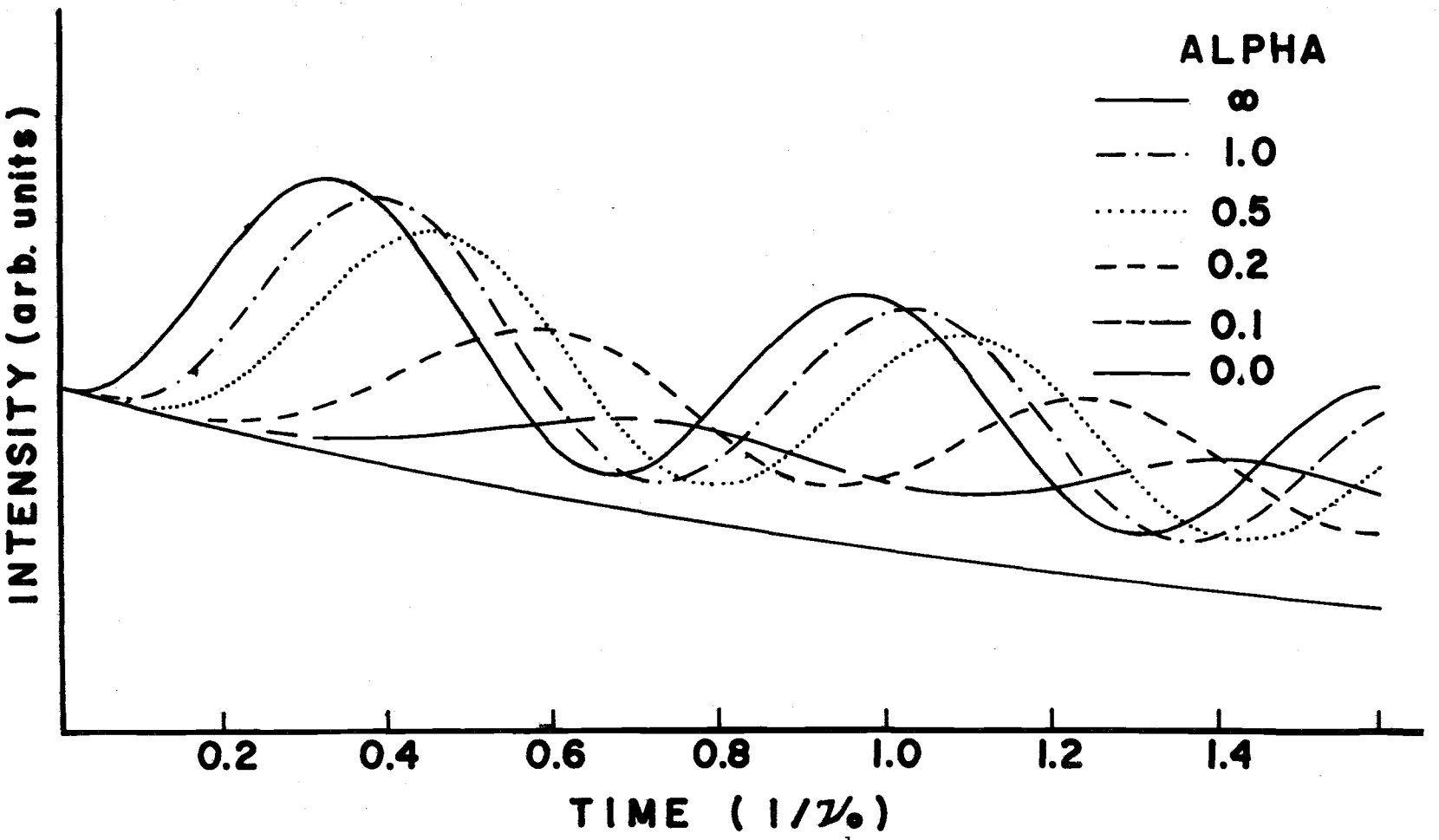

Figure 9a. The calculated effects of the fringing field on a $j = \frac{1}{2}$ system. The atom enters the field region midway between the plates (Figure 8). The varied parameter is $\alpha = \frac{\lambda_0}{\pi d}$ where λ_0 is the beat wavelength of the unperturbed splitting and d is the field plate separation.

unperturbed Lamb shift. For $a > 2$ the beat amplitude approaches the value calculated for the uniform field case ($a = \infty$). For $a \lesssim 1$, however, serious attenuation of the beat results. Also, the beat is phase shifted towards positive times by various amounts depending upon the rise time of the electric field viewed by the atom.

Off axis, similar results are obtained, but the beats are never completely attenuated, since some field always remains at the foil. An interesting case is $y = \frac{1}{4}d$. Here the electric field is constant in magnitude but rotates, as seen by an atom traveling in the positive z-direction, from an initial orientation along the z - axis to a final orientation in the y - direction. For this situation the beat amplitude is minimum for $a \simeq 0.20$ as indicated in Figure 9b.

For the present experiment, $|y| \leq d/8$ and the solution at $y = 0$ is adequate. For Ly-β emission, $\lambda_0 \simeq 1.0$ inch at typical beam velocities. Since $d = \frac{1}{2}$ inch, $a \simeq 0.6$ and it is expected that Stark beats between the $s_{\frac{1}{2}}$- and $p_{\frac{1}{2}}$-levels will be attenuated about 25% and phase shifted about 60°. For Ly-α at the same beam velocity, $a \simeq 0.2$ and the attenuation and phase shift will be 50% and 140°, respectively. These predictions are only approximate because the influences of the $j = \frac{3}{2}$ and $\frac{5}{2}$ states on this beat have been neglected. However, Figure 9a should provide an adequate estimation of the influence of fringing fields on the intensity beats in the present experiment.

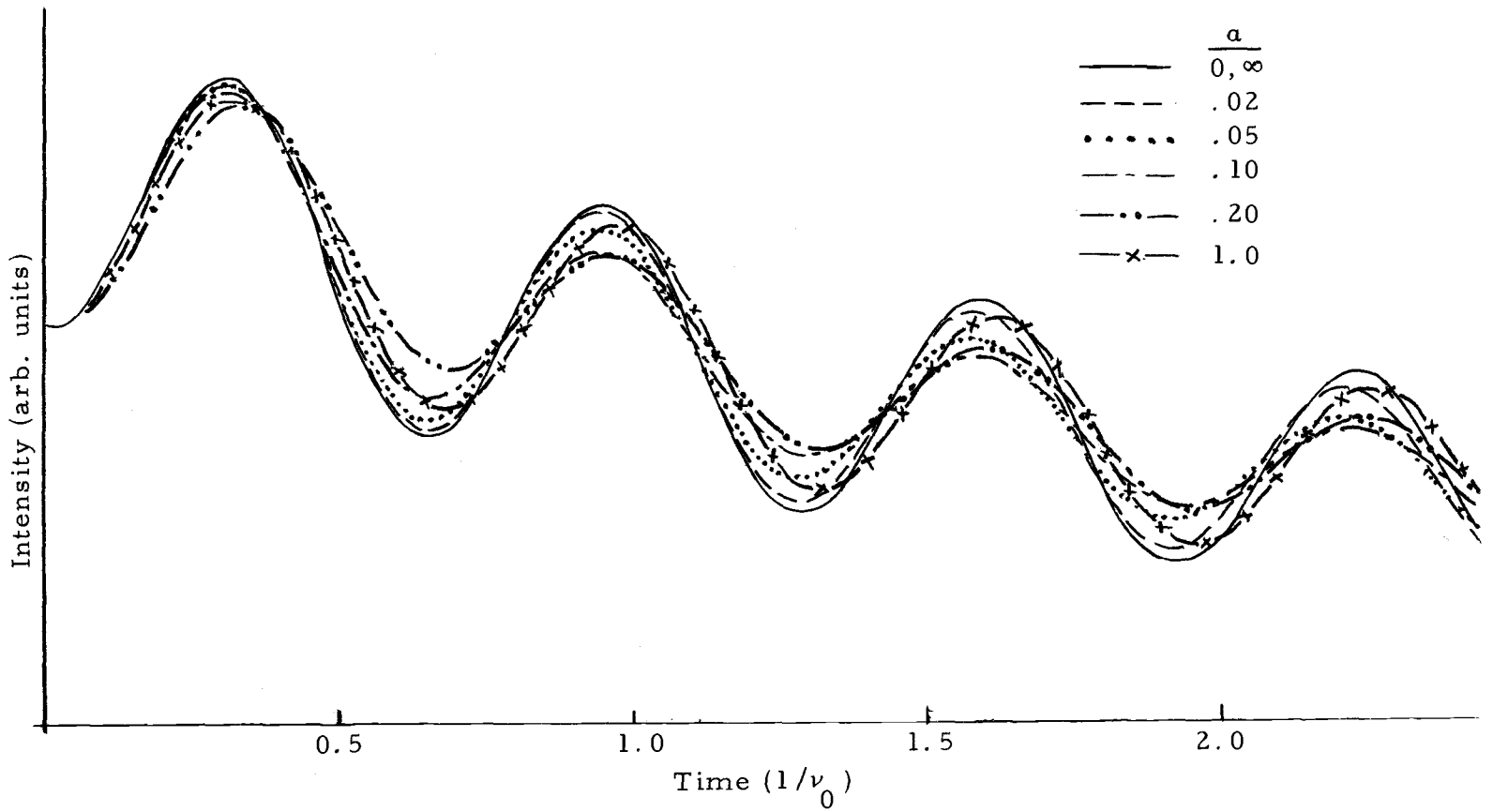

Figure 9b. The calculated fringing field effects for the case where the atom enters the field at y = d/4.

3. APPARATUS

3.1. Beam Source

In order to be able to perform a beam-foil experiment with reasonable intensities of emission lines for hydrogen atoms having kinetic energies in the range from 200 to 500 keV, a beam current of the order of five microamps is needed in the present experiment. The beam source is the four MeV Van de Graaff accelerator (High Voltage Engineering Corp. Model K) at the Nuclear Physics Laboratory of the University of Oregon. Hydrogen molecular ions (H^+, H_2^+ and H_3^+) are extracted from a duo-plasmatron ion source at the high voltage terminal of the accelerator, and accelerated to an appropriate energy. Figure 10 shows a schematic diagram of the ion beam path from the source to beyond the target.

When a beam of ions enters a uniform magnetic field, the radius of curvature for the trajectory is given by $r = \sqrt{2EM}/qB$, where E, M and q are the energy, mass and charge, respectively, of the ions, and B is the magnetic flux density. The field of a bending magnet can therefore be used to select the mass-energy product for a beam of ions. Since the energy of the ions is already approximately determined by the acceleration stage of the Van de Graaff, the bending magnet field strength determines both the mass and energy for ions bent through a given angle. Once the ions with the selected energy

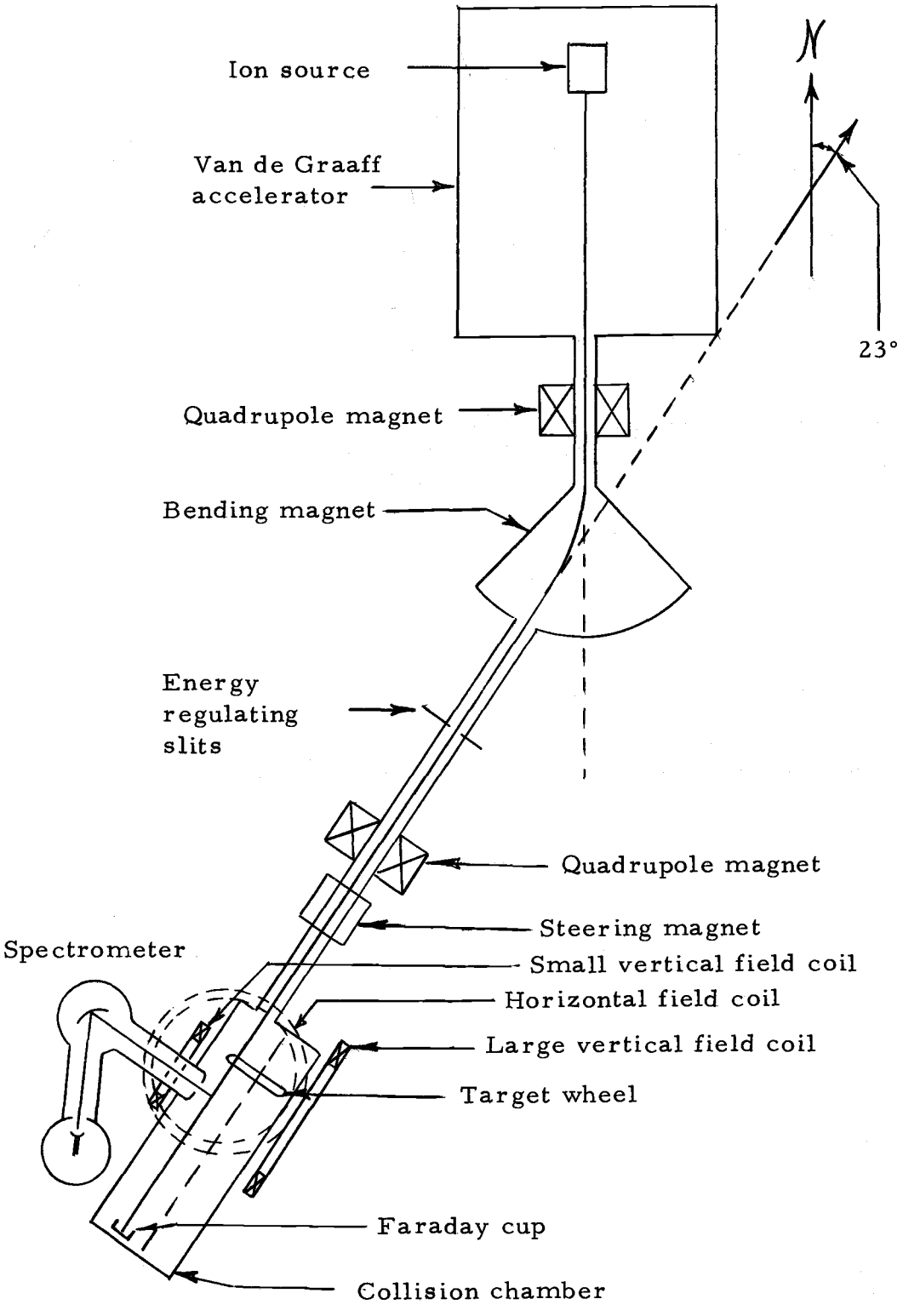

Figure 10. A schematic diagram of the apparatus showing the ion beam path.

and mass pass through the bending magnet, they travel down an evacuated beam tube toward the collision chamber.

A pair of vertical slits are located, and centered, on the beam tube axis approximately five feet down the beam tube from the bending magnet. Each slit blade collects ion current from one horizontal edge of the beam cross section at that point. If the beam energy changes by a small amount, more current falls on one slit and less on the other. The difference in current on these slits is used in a feedback circuit to regulate the acceleration voltage of the accelerator, serving to stabilize the beam energy. This acceleration voltage is the sum of the terminal voltage (as read from a generating voltmeter), the extractor voltage of the source, and the focus ring voltage. The generating voltmeter itself has been calibrated (30) to within an accuracy of ±10 keV.

Electrostatic lenses in the ion source and magnetic lenses (quadrupole pairs) along the beam path are adjusted to focus the beam on a target in the collision chamber. With this particular accelerator, it was found that an additional steering magnet was needed along the beam tube because the beam does not emerge from the acceleration stage at the same point from one run to the next. Small corrections to the horizontal and vertical positions of the beam at the target are made with the steering magnet. The correction angle is always less than three milliradians, so the beam axis and the axis of the collision

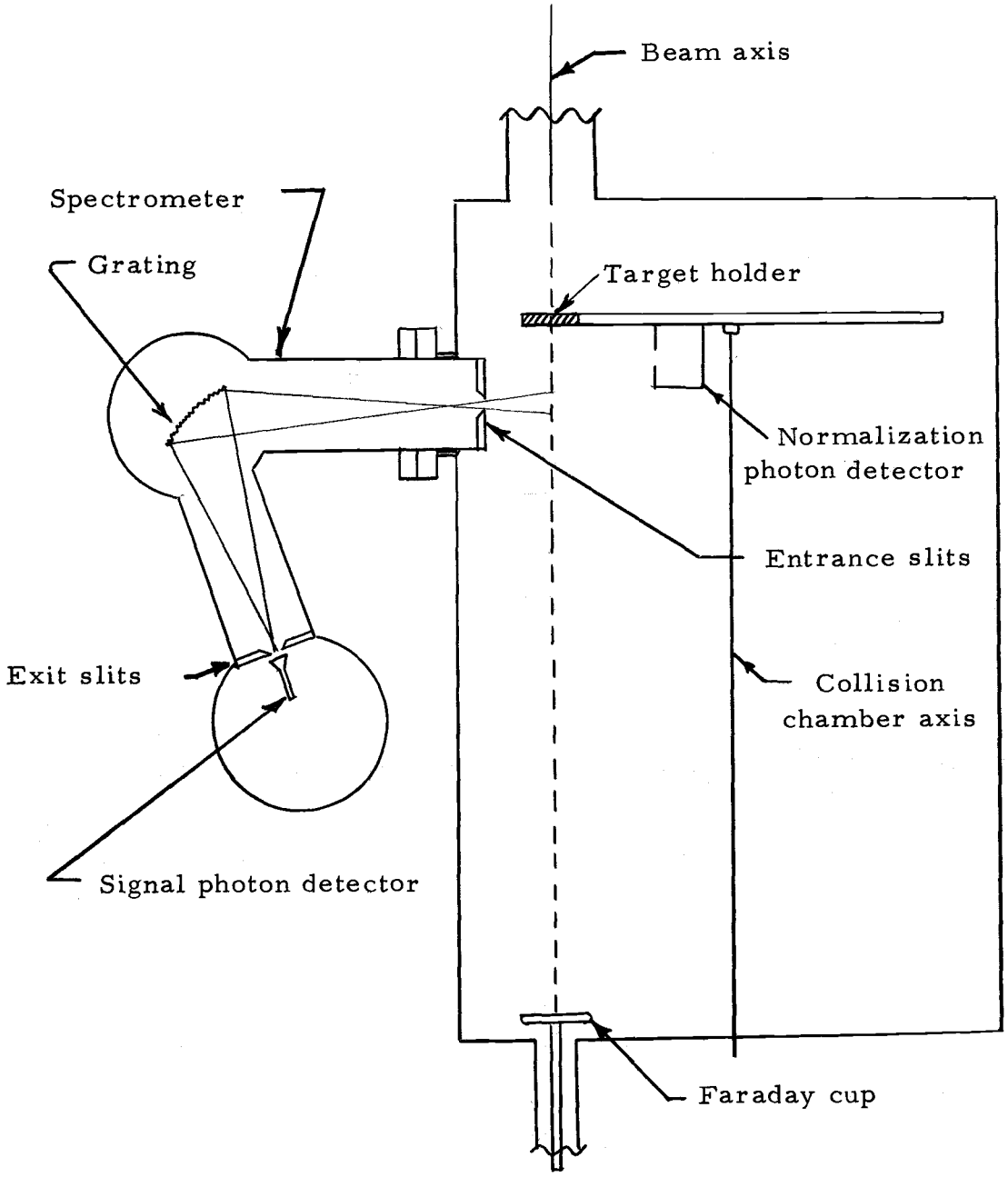

Figure 11. The collision chamber and spectrometer.

beam, this disk gives a visual indication of the beam size and position. The carbon foil targets, which are mounted in pairs, are supported by thin tantalum target holders having a 1/8 inch hole which the foil covers. The purpose of the first foil of the pair is to dissociate the molecular ions; whereas the second foil defines $t = 0$ for the excitation of the hydrogen atoms (13). The two carbon foils are separated by a distance of approximately 0.2 inch. This distance is sufficiently great to insure that the molecular fragments are well separated by the time they reach the second foil (9).

The carbon foil targets, obtained from the Yissum Research Development Co., Jerusalem, are 10 $\mu g/cm^2$ thick. The foil is originally made by sputtering carbon onto a microscope slide. In order to mount the foil on a target holder, it must first be removed from the slide by dipping the slide into water, causing the foil to float to the surface. A drop of household detergent added to the water lowers its surface tension. The foil can then be mounted by slipping a target holder under the foil and carefully lifting the assembly out of the water with the foil and target holder in a vertical plane.

In passing through the foil, the typical beam particle suffers many collisions. Consequently, its energy is degraded by an amount that depends upon the foil thickness, the foil material, and the energy of the beam. Northcliffe (36) has compiled data on the energy losses of protons incident on carbon. Typical energy losses for the foils and

beam energies used in this experiment are 10-20 keV/amu. The correction is uncertain to ±5 keV/amu due to both the uncertainty of the foil thickness and the uncertainty of the published correction factors (36). Since energies of 400 keV/amu are typical in the present experiment, the uncertainty of the foil correction plus the uncertainty of the operating voltage (discussed in the previous section) results in approximately a one-percent uncertainty in the velocity of the emerging beam.

In addition to several carbon foil targets and the quartz target, one empty tantalum target holder is mounted on the target wheel. There is also one position on the target wheel where no target or holder of any kind is mounted, which may be rotated into the beam axis. These last two arrangements allow the beam to reach a Faraday cup at the rear of the collision chamber without any targets being in the path. This is useful for initial adjustment of the accelerator.

For the present work, the Faraday cup is simply a two inch copper disk, centered on the beam axis, which collects the beam current. It is usually biased positively with respect to ground to reduce emission of secondary electrons produced at its surface by the incident beam. The current from the Faraday cup, while not exactly the true positive ion beam current (because of electrons stripped from the foil and carried in the beam (3) and secondary electron emission at the Faraday cup itself), is proportional to the beam current. Since

the number of atoms per unit length of the beam downstream from the foil is proportional to the Faraday cup current, the intensity of Lyman-β radiation measured by the spectrometer is also proportional to this current.

3.3. Spectrometer

As shown in Figure 11, the spectrometer assembly is mounted on a flange of the collision chamber such that it views a section of the beam at 90° to the beam axis. The spectrometer is a 0.5 meter Seya-Namioka type (33) with a McPherson Co. gold replica grating of 1200 lines per millimeter, blazed for 1500 Å. The unit, which was locally designed and constructed, has a linear reciprocal dispersion of 16.6 Å/mm. An external drive allows the grating to be rotated, with the unit under vacuum, to investigate radiation from the visible to the extreme ultraviolet region of the electromagnetic spectrum. As used in the present experiment, the grating is positioned such that Lyman-β (1026 Å) or Lyman-α (1215 Å) radiation passes through the exit slits. The entrance and exit slit widths are .045 inch and .050 inch, respectively.

These slit widths, as well as the finite acceptance angle of the spectrometer, determine the detector slit function, $f(t, t')$, as defined in Section 2.3. The slit function for the spectrometer was measured in an earlier experiment (8). A description of this

measurement can be found in Appendix B. Basically, the slit function is found to be nearly triangular with a full width at half maximum of approximately 0.063 inch. This measurement is in agreement with the calculated slit function based upon the known umbra-penumbra as determined by the grating width and the entrance slit (32).

The finite slit widths of the spectrometer limits not only the spatial resolution of the detection system, but also the spectral resolution. If the exit and entrance slits are opened too much, the broadened Ly-β and Ly-γ lines may overlap. Figure 12a is the observed spectrum of the background gas excited in an ionization gauge placed directly in front of the spectrometer entrance slits. The spectrometer slits, in this case, are nearly closed and the observed linewidths are about 5 Å, FWHM. With the spectrometer slits opened to 0.045" and 0.050", the spectrum shown in Figure 12b is obtained. The linewidths in this case are 25 Å, FWHM. At these slit widths the Ly-β and Ly-γ lines are just resolved, as is required.

The intrinsic polarization of the spectrometer was also measured in a previous experiment (8). It was found that the spectrometer favored Ly-β light polarized parallel to the grating's rulings by a factor of 3.4 ± 3 compared with light polarized perpendicular to the rulings. The measurement of this factor is described in Appendix A. For Ly-α emission, it is assumed that the same polarization factor applies. This is a reasonable assumption since the optical properties

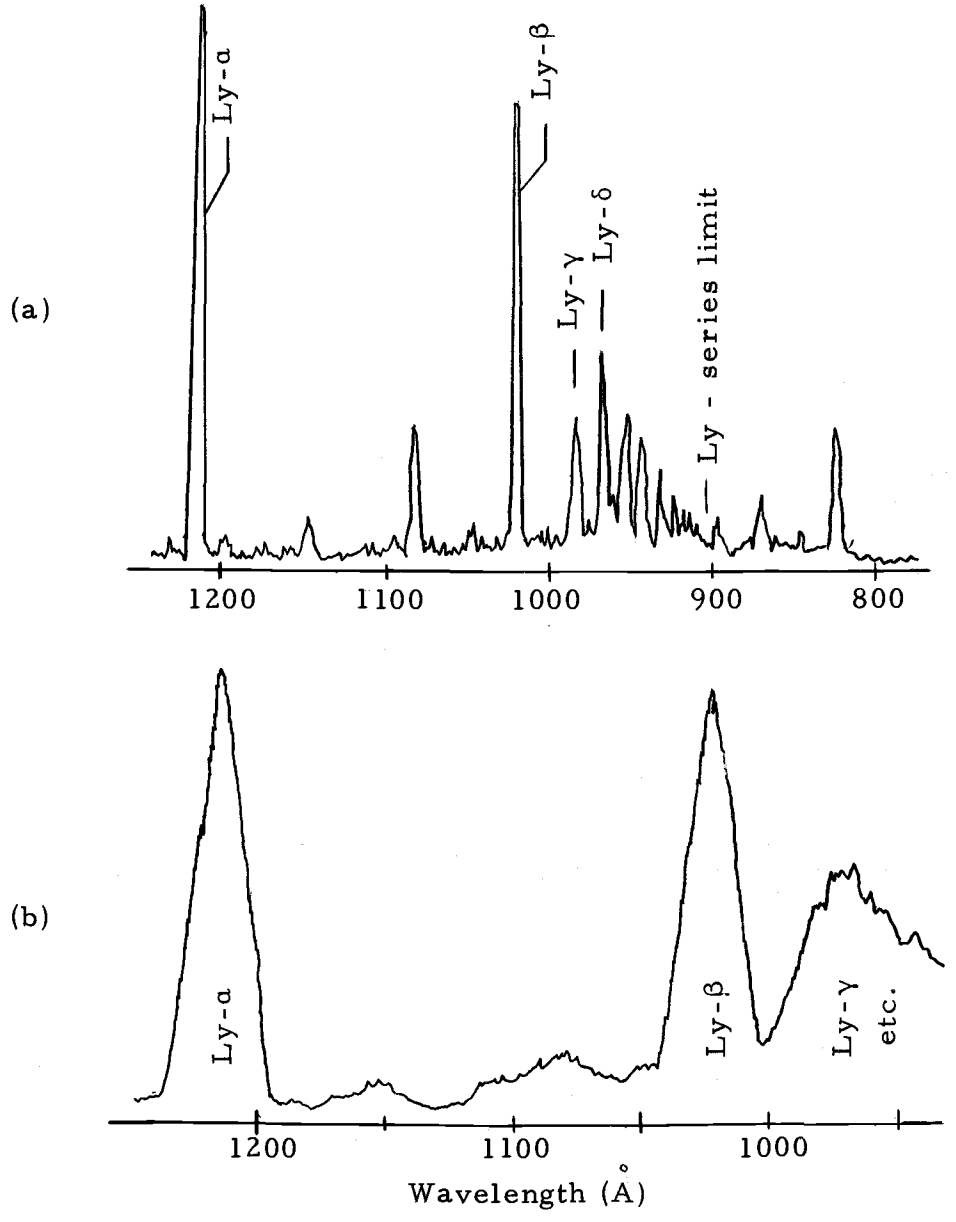

Figure 12. The spectrometer resolution.
a) Spectrum of the excited background gas with the spectrometer slits nearly closed.
b) The same spectrum with the spectrometer slits opened, as used in the present experiment.

of gold do not vary greatly over this frequency range (33).

The distance between the foil position and the center of the field of view of the spectrometer is only determined to within an additive constant by the micrometer setting alone. The measurement of the absolute positioning of the foil relative to the spectrometer is discussed in Appendix C. It is found that a micrometer setting of 8.266 inches corresponds to the absolute position at which $t = 0$, to within 0.010 inch.

3.4. Detectors

At the spectrometer exit slit a Bendix Channeltron Photon detector, Model 4028, counts ultraviolet photons. A Channeltron detector (34) is basically a hollow helix attached on one end to a small cone which serves as a photocathode. This entire device is made from a lead glass material which has a work function similar to that of Tungsten. Figure 13 shows a diagram of the detector and the circuitry used in conjunction with it. When photons with wavelengths less than 1500 Å strike the photocathode, electrons are emitted from this surface. The quantum efficiency (number of photo electrons per photon incident on the photocathode) is 6% at a wavelength of 1026 Å (35). An electric field, produced by the potential difference applied across the entire length of the Channeltron (which has a resistance of about 10^9 Ω) accelerates these electrons down the inside of the helix.

Each time electrons strike the inner wall of the helix, secondary electrons are emitted, producing electron multiplication. Thus, each initial photoelectron is multiplied into a short pulse of electrons at the positive voltage end of the helix. A nearby anode is biased to collect this electron pulse, which is typically of the order ten picocoulombs. This charge pulse, in turn, is converted into a voltage signal by a charge sensitive preamplifier. The voltage pulse out of the preamp is amplified and counted using standard pulse counting circuitry as is discussed below. The electron gain of the Channeltron is nominally 10^8. Its pulse height distribution is approximately Gaussian with a full width at half maximum of fifty percent at this gain.

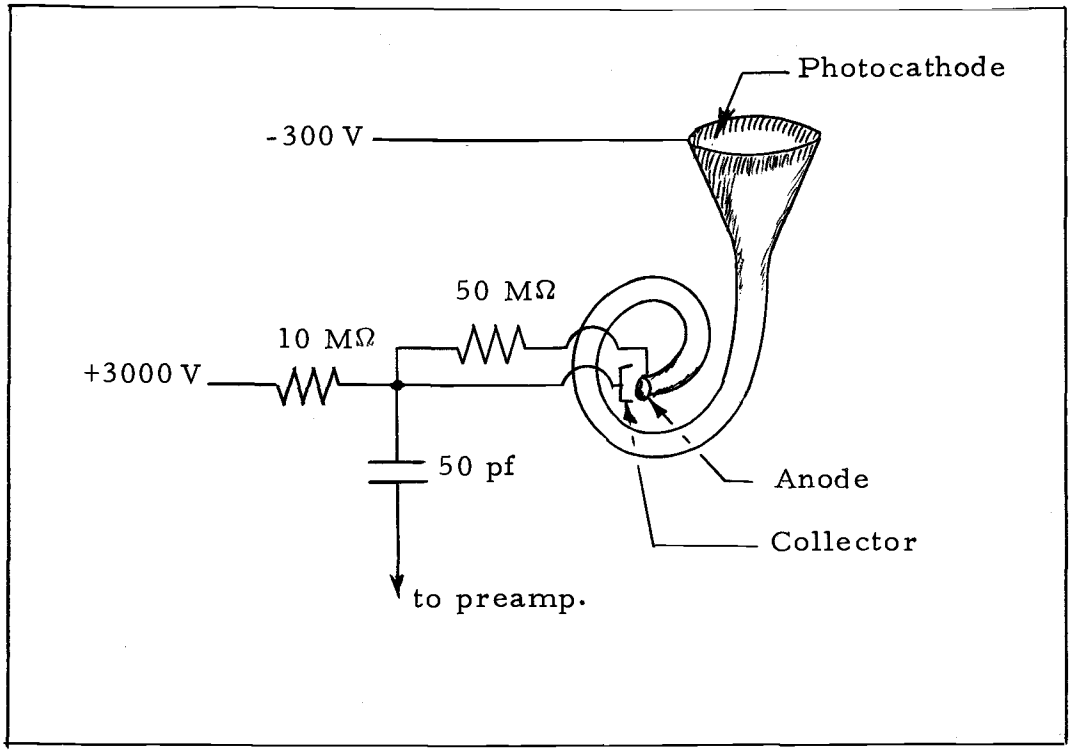

Figure 13. The Channeltron photon detector circuit.

Since a Channeltron detects electrons incident on the cathode with approximately 100% quantum efficiency and Lyman-β photons with 6% quantum efficiency, it is necessary to bias the cathode 300 volts negative with respect to ground. This bias prevents low energy electrons from reaching the photocathode. These low energy electrons are produced both in the foil, by momentum transfer with the beam, and by the ultraviolet radiation incident on various surfaces in the spectrometer (33).

Two important advantages of a Channeltron detector over other photon detectors for extreme ultraviolet radiation, are its narrow pulse height distribution (for single event detectors), and its low dark current (output pulses with no signal radiation incident on the photocathode), which is less than five counts per minute (31). Because the dark current count rate is so small, there is negligible background due to the detector in signal count rate data.

3.5. Electronics and Control Logic

There are four quantities which are recorded during a data run at a given position of the foil along the beam axis: the integrated beam current, the signal counts from the Channeltron detector at the exit slit of the spectrometer, the counts from the Channeltron detector which moves with the foil, and the real time interval for counting. The last three quantities are normalized to a fixed value of

the first. Figure 14 shows a block diagram of the circuitry used for data acquisition.

The output from each of the photon detectors is a charge pulse which is converted to a voltage pulse by a Hewitt Packard Model 5554A charge sensitive preamplifier. This voltage pulse is amplified by a linear voltage amplifier (Tennelec model TC 213) and the amplified voltage pulse is fed through a discriminator. The discriminator gives a logic pulse output if the input voltage pulse is greater than the fixed discrimination voltage of the unit.

The current from the Faraday cup is fed into a current integrator-digitizer (Ortec model 439). The count rate of logic pulses out of the integrator-digitizer is proportional to the current input. A pulser (Tennelec model TC 812), which outputs 60 counts per second, acts as a real time clock.

The logic pulses from the linear amplifiers, the current integrator/digitizer, and the 60 Hz pulser are the four inputs to a master logic unit, and also to four display scalers slaved to the logic unit. This unit was locally designed and built, utilizing logic modules manufactured by Digital Equipment Corporation. Basically the unit has four functions: 1) It stores each input pulse in the proper channel of a Northern Scientific (Model NS-630) Memory Unit with a prearranged priority (signal pulses taking preference in case of coincidences); 2) it controls the duration of each data interval by counting a

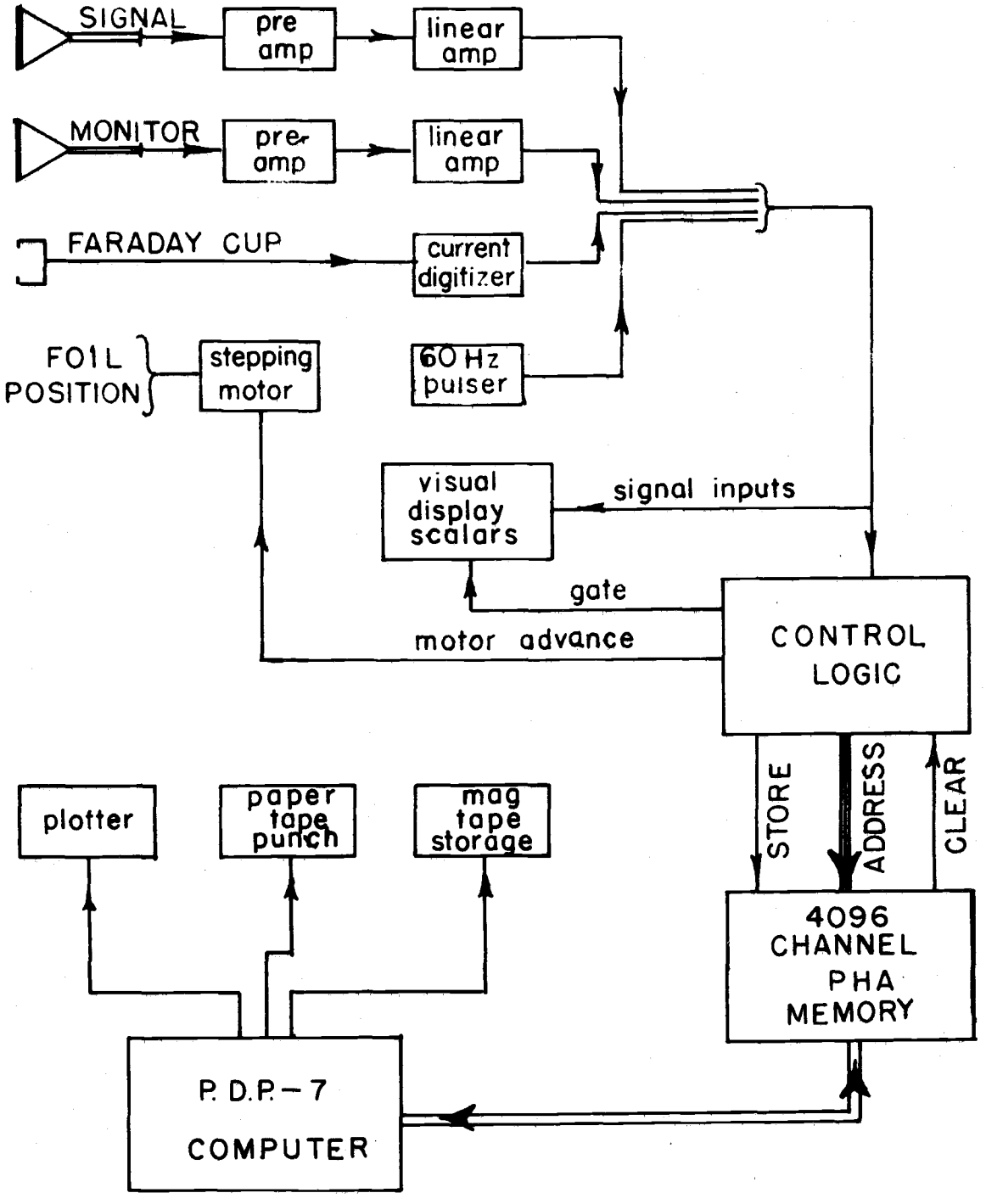

Figure 14. A block diagram of the control and signal recording electronics.

preset number of pulses from a selected input; 3) it automatically advances the foil position between data intervals; and 4) it resets the slaved scalers and automatically begins a new data interval after a short pause (~1 sec) following the foil advancement. The memory unit is divided into quarters of 1024 channels each. Only one quarter is utilized during a particular data scan, as manually selected by means of a switch on the memory unit. The logic unit further subdivides the available 1024 channels into quarters of 256 channels each. Each of the four inputs are stored in a different 256 channel region. The least significant eight bits of the channel address are determined by the foil position. This part of the address is incremented one channel, by the logic unit, each time the foil is advanced. Thus, in a typical data scan, channels 1-60 correspond to the integrated Faraday cup current at each of the 60 foil positions, channels 257-316 contain the elapsed times of each data interval, channels 513-572 contain the monitor counts, and channels 769-828 contain the actual signal counts.

Since the duration of each data interval is determined by counting a preset number of pulses from the Faraday cup current integrator, this input should remain constant for each foil position. There is a small possibility that simultaneous pulses from two inputs will arrive at the logic unit. Since only one input can be stored at a time in the memory unit, one of these pulses may be lost. This possibility was reduced by inclusion of a one pulse memory in the logic unit; however,

multiple coincidences would still result in lost pulses. A measure of the number of lost pulses is the difference of the recorded Faraday cup counts and the preset value. This difference is always found to be less than 0.1 percent.

Up to four data scans can be stored in the memory unit. To make room for additional scans, the data must be transferred to magnetic tape. This is done via a PDP-7 computer which interfaces with the memory unit.

The computer also allows a preliminary analysis of the data. A computer routine which displays the data on a cathode ray tube and has some editing capabilities is used to survey the various recorded signals. Thus, problems such as beam instabilities, excessive backgrounds, or foil deterioration can be quickly established. A point plotter gives a permanent, visual record of the displayed data.

When all scans have been completed and stored on magnetic tape, the data are transferred to paper tape for permanent record. This tape is then input into the OSU computing facility for extensive analysis, as described in Section 4.3.

3.6. The Magnetic and Electric Fields

The purpose of this experiment is to obtain relative cross sections for excitation of the atom into its possible ℓ, m_ℓ levels. As discussed in Section 2.2b, this can be obtained from an analysis of the

decay pattern of emitted radiation in a uniform electric field. A particle moving in a magnetic field, $\vec{B}$, experiences a motional electric field

$$\vec{E} = [1-(\frac{v}{c})^2]^{-1/2} \frac{\vec{v}}{c} \times \vec{B}, \qquad (36)$$

where $\vec{v}$ is the particle's velocity. Since static electric fields of the desired uniformity are difficult to obtain, motional electric fields are utilized, for the most part, in the present experiment.

The amplitude of a quantum beat between two levels of opposite parity is proportional to the square of the mixing of these levels in the electric field (28, 29). For the $n = 2$ levels of hydrogen, fields of 400 V/cm or more will largely mix the $s_{\frac{1}{2}}$- and $p_{\frac{1}{2}}$-levels. For $n = 3$, the corresponding levels are comparably mixed in fields of 50 V/cm or greater. The larger the mixing of two levels, the more accurately the relative initial populations of the levels can be determined.

To obtain a motional field of 50 V/cm, a magnetic field of approximately five gauss is required, at the beam velocities typical of the present experiment. To obtain such a field, a 36-inch diameter 287 turn coil was positioned vertically, parallel to the beam axis, approximately 15 inches from the target region. The resulting magnetic field was measured using a Hewlett Packard Magnetometer

Probe (H.P. 3529A). The magnetometer probe, attached to the target wheel in place of a foil, was translated along the beam and the magnetic field, as a function of the target position, was recorded. The measured magnetic field is found to be uniform to within one percent over a six inch region along the beam axis, immediately upstream from the spectrometer. Fields up to nine gauss can be obtained with this coil.

For Ly-α data a much larger field is needed. Therefore, a 12 inch diameter, 200 turn, #16 wire coil was also constructed. This was placed parallel to the first coil but somewhat closer ($\simeq$ 8 inches) to the target region. Fields up to 50 gauss ($\sim$ 400 V/cm) can be obtained with this coil. Again the field is found to be uniform to within one percent, but only over a two inch interval along the beam axis. This distance is sufficient for Ly-α since the $n = 2$ splittings are approximately a factor of three greater than those found for $n = 3$.

To control the vertical component of magnetic field, a second large coil was positioned horizontally above the target region. By means of this coil it is possible to compensate for the vertical component of the Earth's magnetic field to within 50 milligauss over the entire target region. Vertical fields up to five gauss can also be obtained with this coil when desired.

An absolute calibration of the magnetic field produced by each

coil, as a function of its current, was obtained using the magnetometer probe. The probe itself was calibrated by measuring the field at the center of an isolated coil with a precisely known current passing through it.

During a data run, the magnetic field present is determined from the current in each coil, using the calibration curves. A total uncertainty of ±1% is assigned these fields, due primarily to uncertainty in measuring the coil current and, secondarily, due to the small variation of field with position. The motional electric field present is then calculated from Equation (36). No attempt is made to control the component of the magnetic field along the beam axis since it can produce no motional electric field.

In experiments on Stark perturbed Ly-α decay, Andrä (11) observed little or no beat amplitude in an electric field (between condenser plates) perpendicular to the beam. The equivalent motional electric field, however, always produced beats. In principle the two measurements should differ only in the effect that the magnetic interaction has on the atom. Since this effect is quite small compared with the Stark perturbation, the discrepancy reported by Andrä (11) is disturbing. Therefore, it was decided to repeat this comparison of beats observed in electrostatic and motional electric fields, both for Ly-α and Ly-β emissions.

Figure 8 is a schematic illustration of a foil holder-field plate

assembly constructed for this purpose (the configuration is similar to that employed in Andrä's experiment). The entire device is made of non-magnetic materials to insure that the magnetic coils could be utilized independent of the presence of this assembly in the target region. Using the nomenclature of Section 2.5c, an applied potential, 2V, across the plates produces a nominal electric field of 2 V/d. Since the foil holder is metal, this field is strongly perturbed near the foil, but is accurate for $z \gg d$. The effect of the nonuniformity of the field near the foil is discussed in Section 2.5c.

4. EXPERIMENTAL TECHNIQUE AND RESULTS

4.1. General Procedures

The first step in any beam-foil experiment is to obtain in the collision chamber an ion beam of the desired energy, physical size and intensity. Section 3.1 describes the path of a beam from the ion source to the collision chamber. In the chamber, the beam size and position are determined visually by inserting a quartz disk target into the beam path, since quartz fluoresces when struck by the beam. Final beam focus is achieved by minimizing the beam spot size on the quartz and maximizing the Faraday cup current with no target in the beam path. Typically, the beam forms a spot of approximately 0.25 inch diameter on the quartz. The Faraday cup current is usually five to ten microamperes. It should be mentioned that the ion beam dimensions do not vary appreciably along the beam axis over several inches. During an actual data scan the foil traverses a maximum distance of about six inches (two inches for Ly-α) along the beam axis.

Having obtained a good beam, the field coils are adjusted for zero magnetic field in the target region and a preliminary data scan of Ly-β radiation is then taken. There are four quantities which are recorded at a given position of the foil along the beam axis: the integrated beam current, the signal counts from the Channeltron detector at the exit slit of the spectrometer, the counts from the

normalization Channeltron photon detector, and the real time interval for counting. The last three quantities are normalized to a fixed value of the first. With this method of normalization any fluctuations in beam intensity do not affect the counts from the signal detector. The counts from the normalization detector (Channeltron) remain constant if foil properties do not change. The real time measurement serves as a check on long term stability of the beam. A preliminary data scan amounts to recording the four above mentioned quantities for values of z from -0.5 inches to 5.0 inches at 0.1 inch intervals (see Figure 1). This provides a quick check on the beam and the experimental apparatus by tracing out the exponential decay of the 3p states of hydrogen. Another consistency check used is to repeat this scan with the spectrometer adjusted to pass Ly-α radiation (1215 Å) and to trace out the exponential decay of the 2p states.

After completing a preliminary data scan, the magnetic field is adjusted to the desired value, the spectrometer is adjusted to the desired wavelength, and an actual data scan is begun. For a typical scan of Ly-β emission, data are taken over a range of approximately six inches beginning at $z = 0.0$ and advancing the foil in increments of 0.10 inch. For Ly-α emission, because of the higher frequencies and shorter lifetimes involved, only about two inches are covered, in intervals of 0.03 inch.

Data are taken at each position for a real time interval of 20-60 seconds, depending upon the count rate. Total scan times of approximately one-half hour are short enough to minimize the effects of accelerator drifts or foil aging. Counts per channel of 5-20 thousand are sufficient to keep statistical uncertainties smaller than other sources of error.

After a preset count is recorded for the integrated Faraday cup current, the target wheel (i.e., foil) is advanced automatically to the next position. Data are displayed on scalers and automatically recorded in the memory of a pulse height analyzer as described in Section 3.5. A single data scan consists of the data recorded for the 60 or so values of z (the distance from the foil to the field of view of the spectrometer) spaced the present distance apart.

A complete data run at a particular beam energy consists of Ly-β scans recorded at several values of the vertical motional electric field. Comparison scans with equivalent fields, except oriented horizontally, or vertical fields using the electric field plates described in Section 3.6, were also taken in some cases. Ly-α data was also collected in some of the latter runs.

4.2. Data

Figures 15-21 are samples of data taken at various energies and in various field configurations. The curve fitting results, where

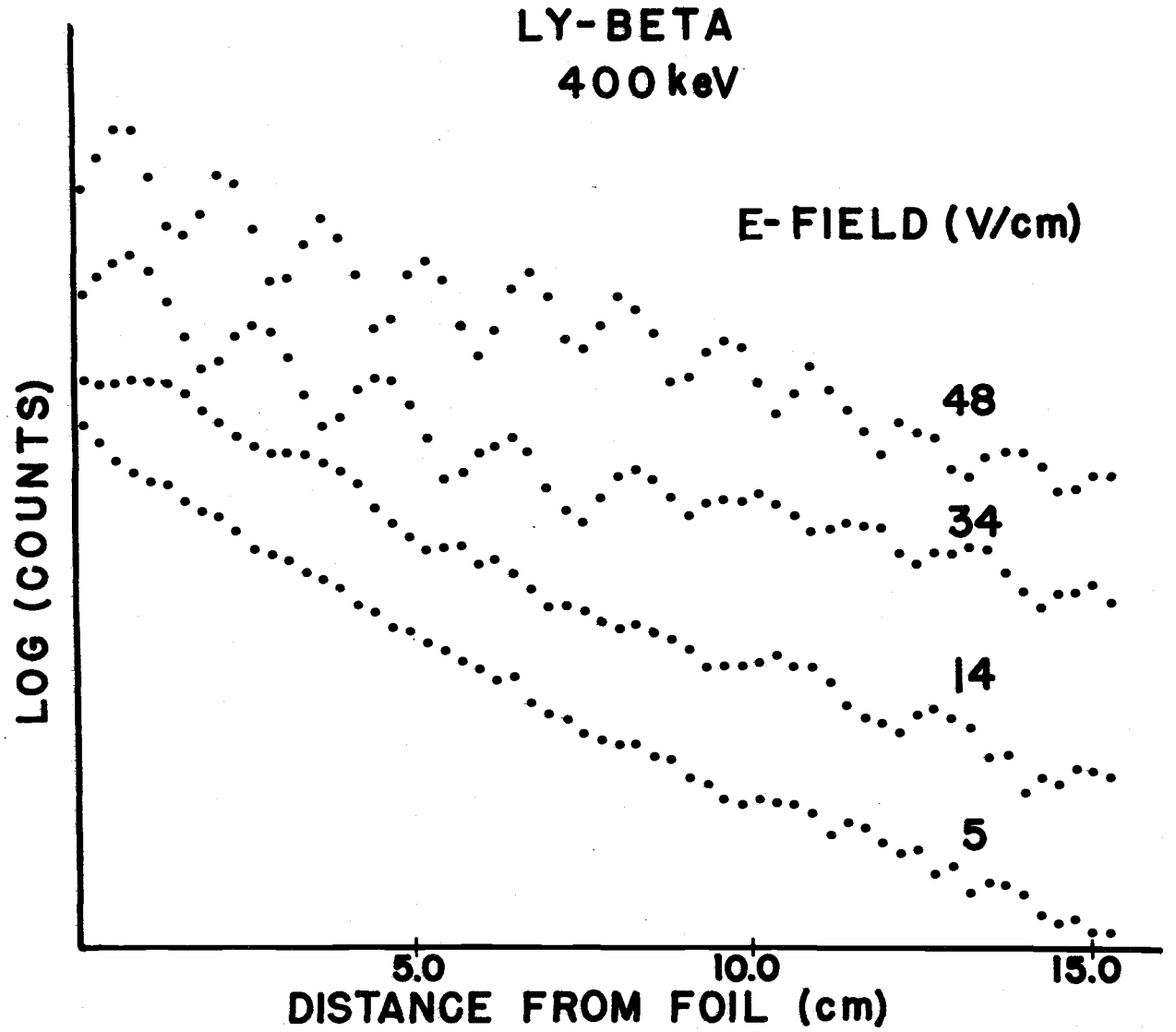

Figure 15. Experimental data for Ly-β emission at 400 keV energy per hydrogen atom.

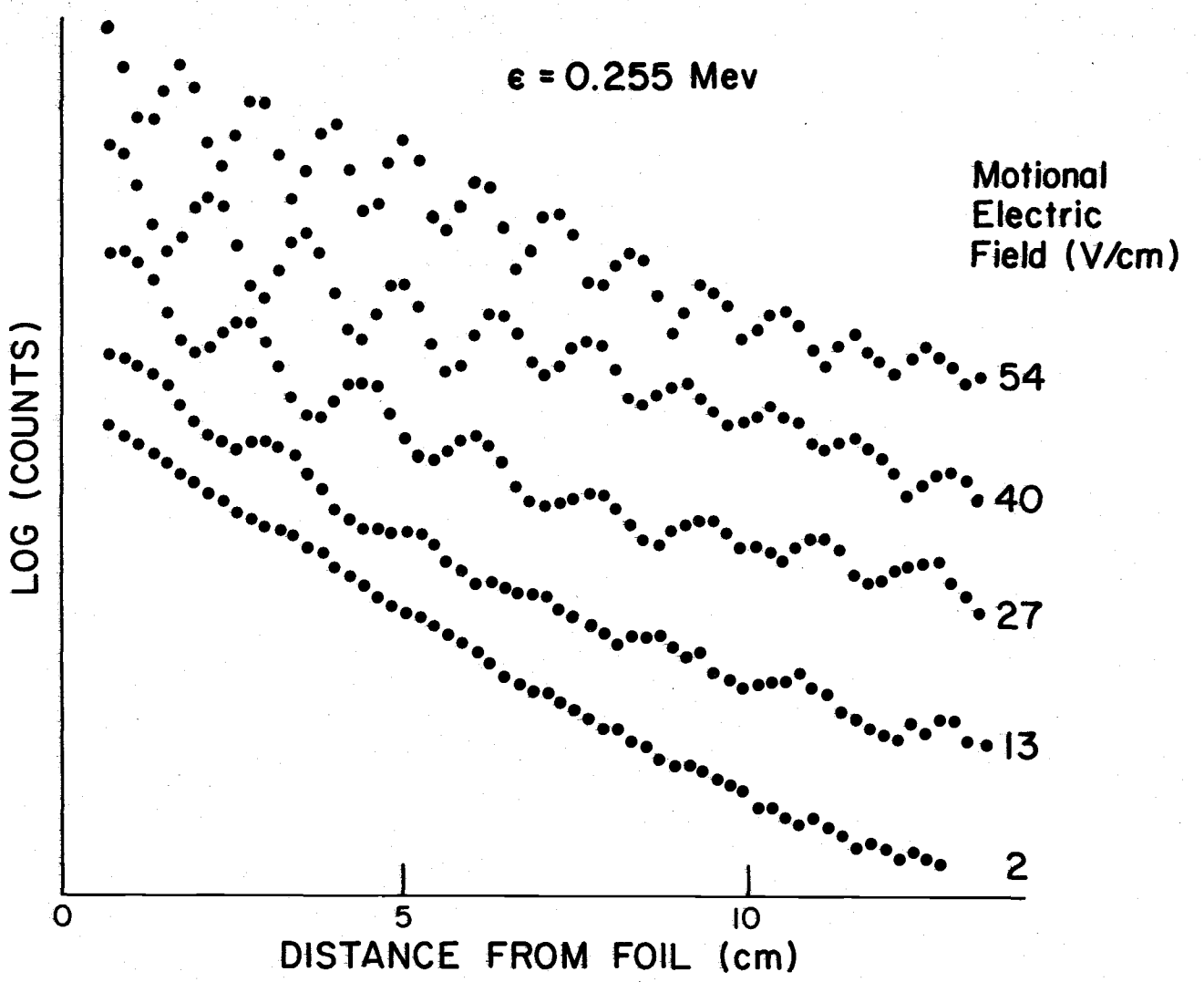

Figure 16. Experimental data for Ly-β emission at 255 keV energy per hydrogen atom.

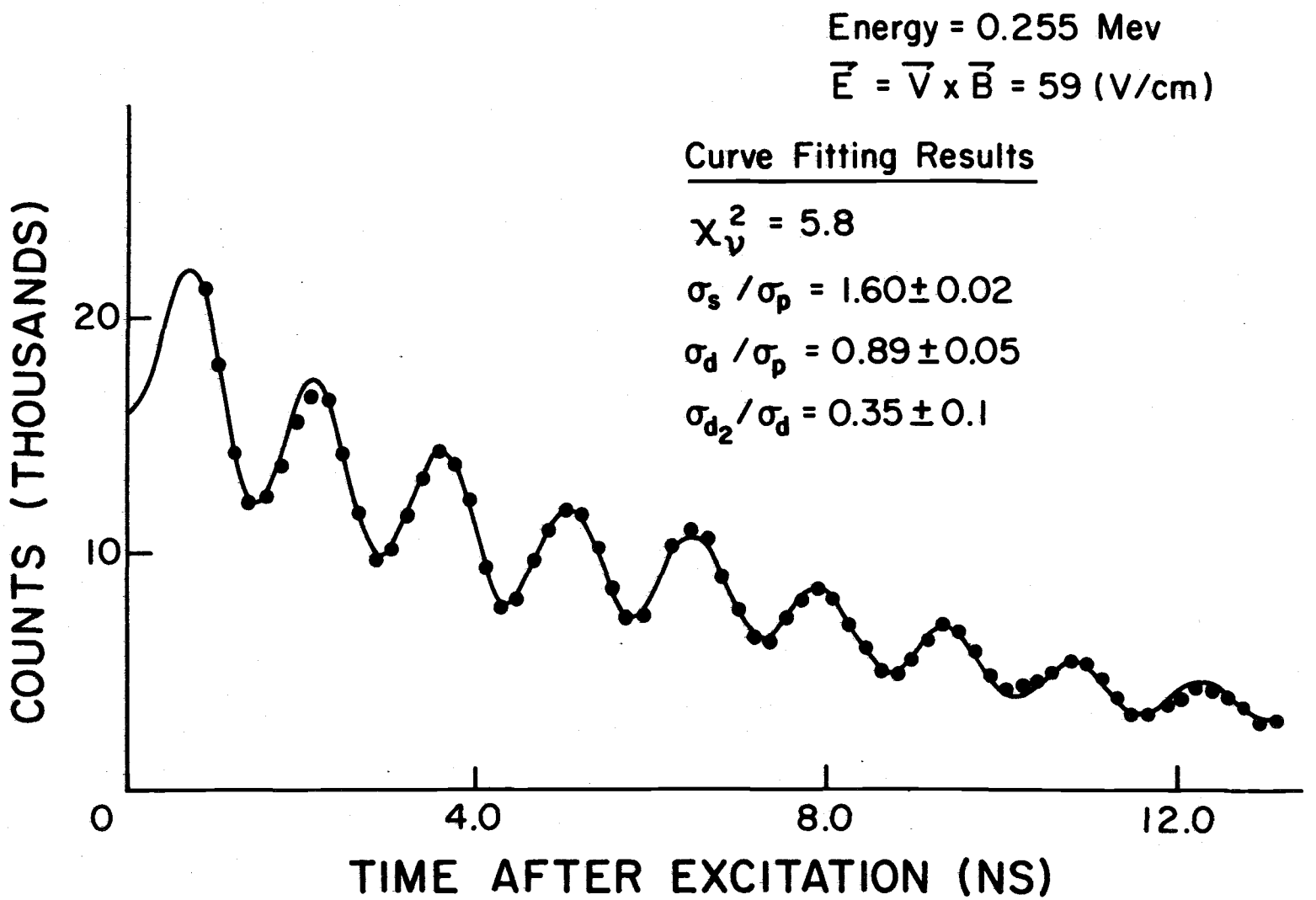

Figure 17. The computer fit to the observed Ly-β emission in an electric field of 59 V/cm. The uncertainties listed are due to statistics only.

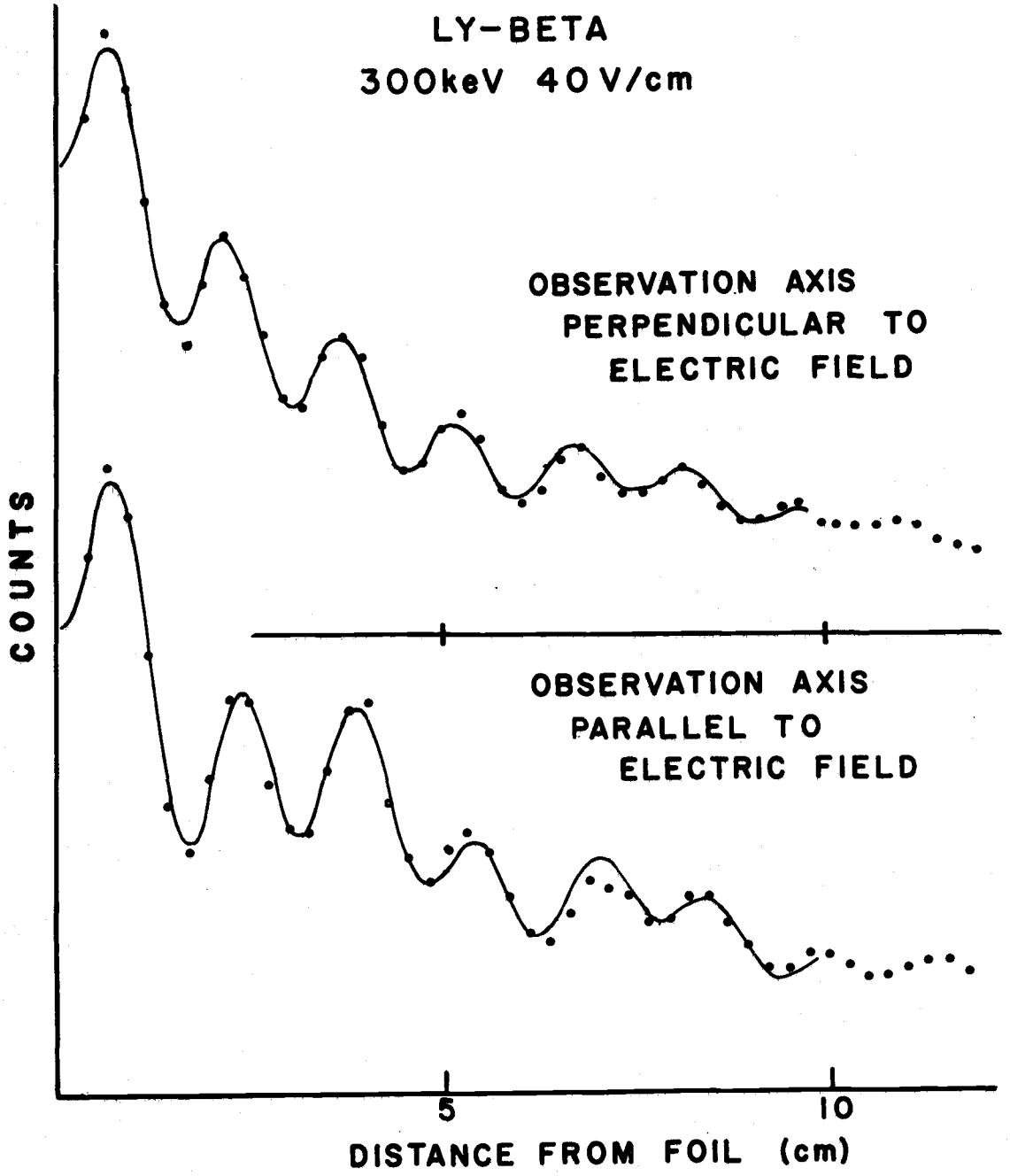

Figure 18. A comparison of Ly-β emission with different field orientations. The motional electric field is 40 V/cm. The solid curves are independent computer fits to the two patterns yielding results consistent to within the fitting uncertainties.

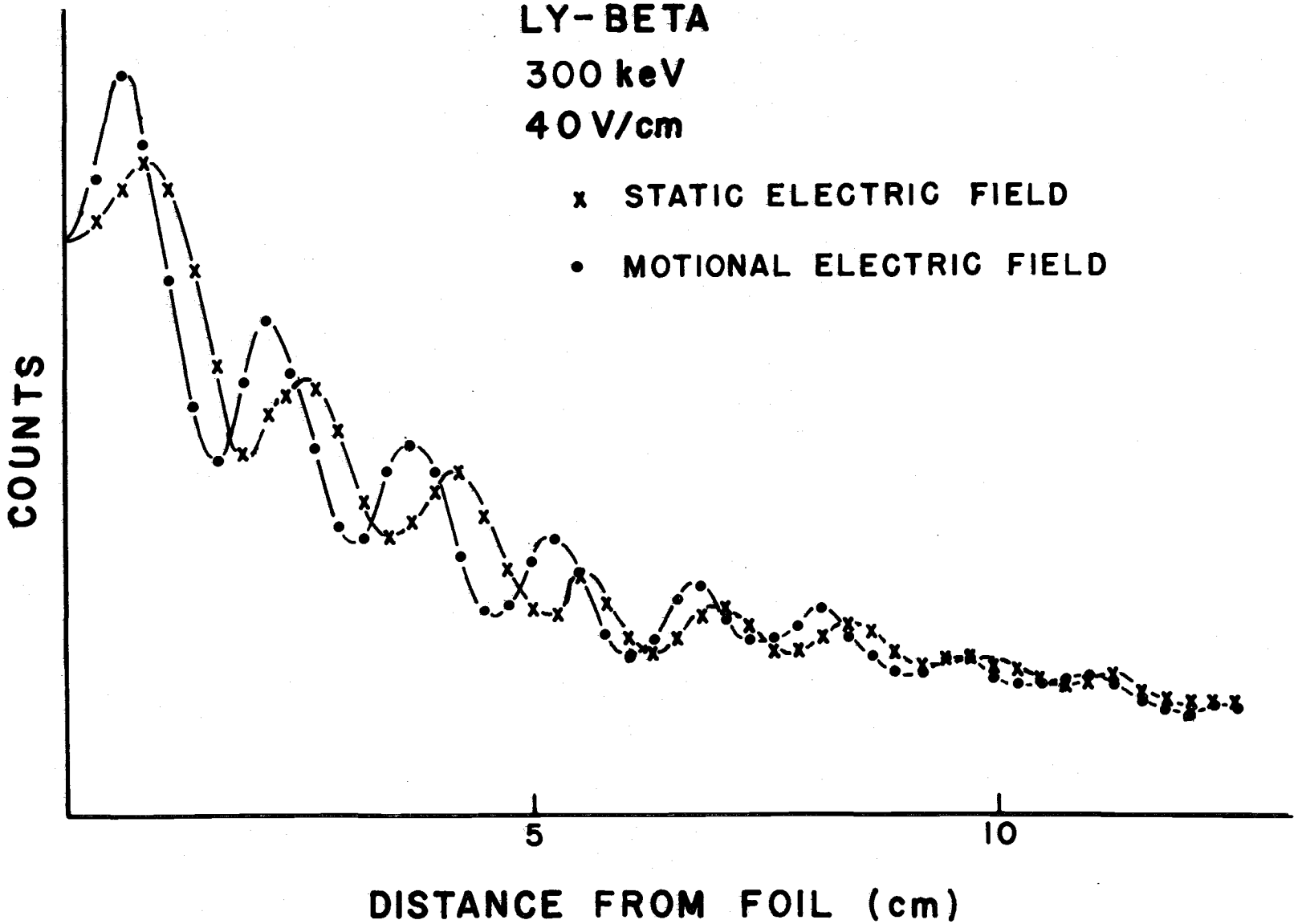

Figure 19. A comparison of Ly-β emission in static and motional electric fields. The curves connecting data points are a visual aid only.

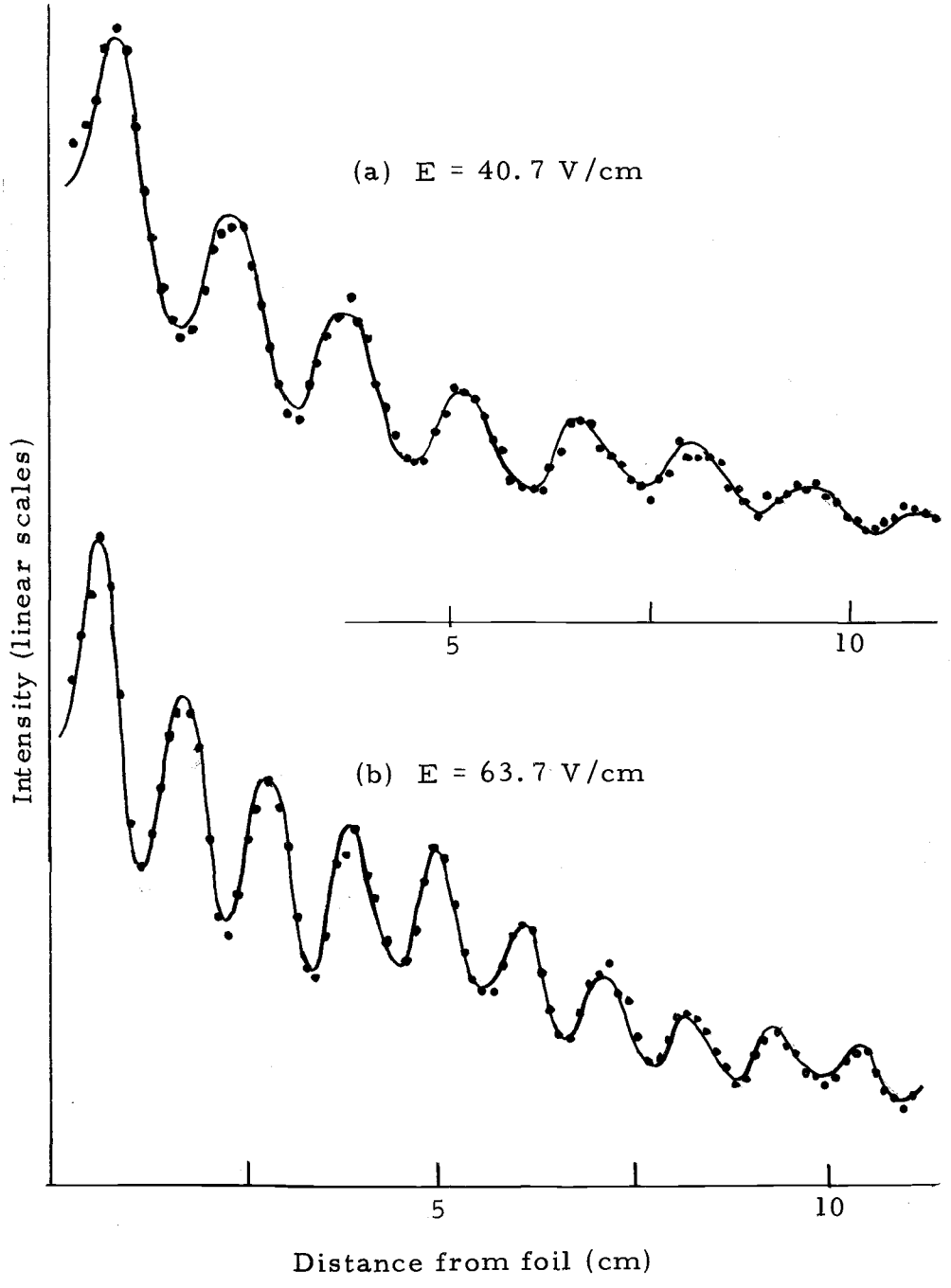

Figure 20. Independent computer fits to Ly-β emission at two field strengths. The curve fitting results are consistent to within the experimental uncertainties. The beam energy is 340 keV/atom.

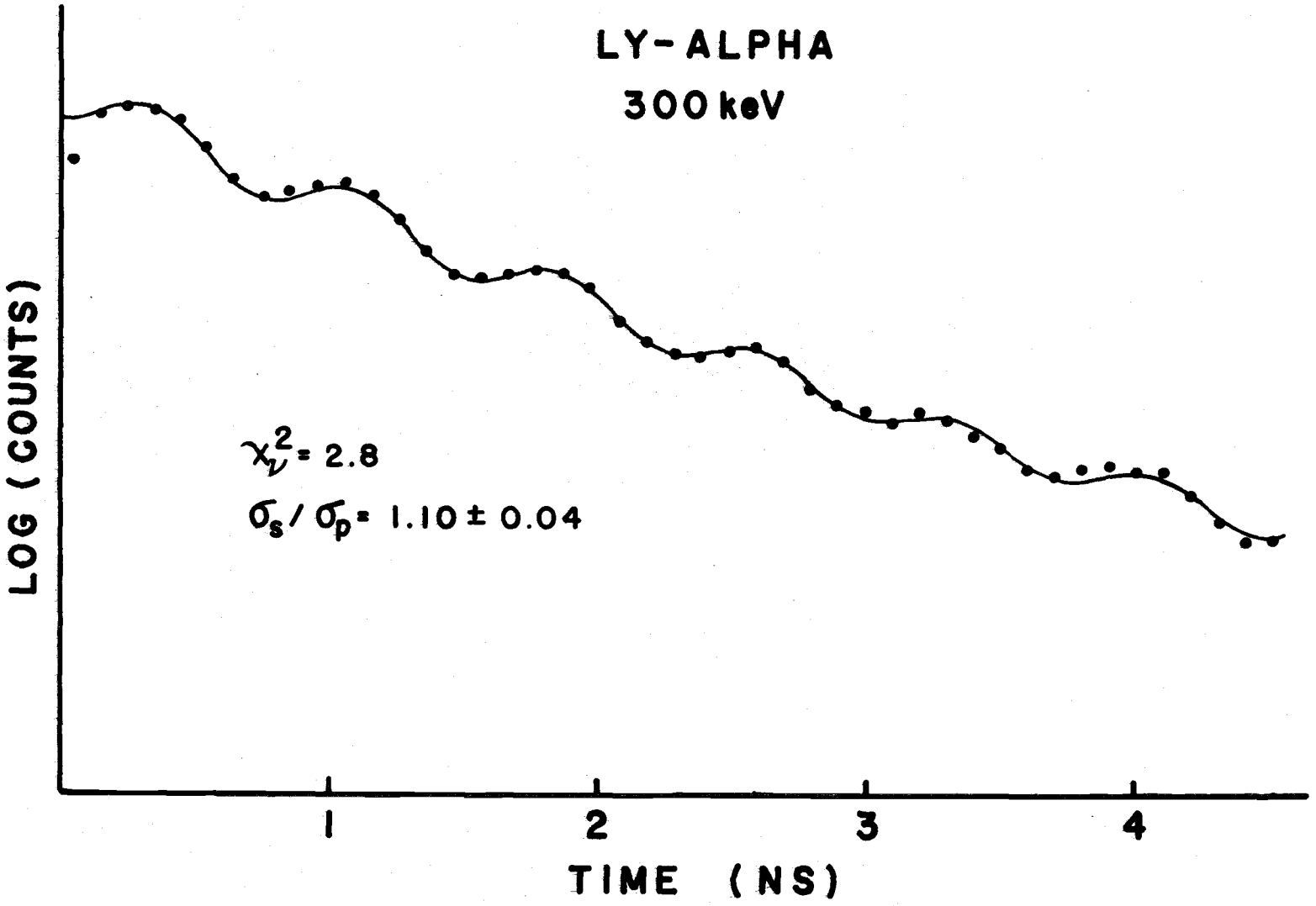

Figure 21. Stark beats in Ly-α emission. The motional electric field is 200 V/cm.

indicated, are discussed in the next section. In addition to the data shown, runs were also taken at 305, 340 and 508 keV.

It is seen by inspection that the decay curves just described are approximately of the form of a monotically decreasing function with a superimposed sinusoidal component. Furthermore, the frequency of the oscillating component corresponds, roughly, to the frequency of the Stark-perturbed $s_{\frac{1}{2}}$-$p_{\frac{1}{2}}$ Lamb shift illustrated in Figure 3. In all cases it is found that the oscillating component is at its minimum value at the foil position. On the basis of this last observation, it is concluded that the $s_{\frac{1}{2}}$-levels are preferentially populated compared with the $p_{\frac{1}{2}}$-levels (see Section 2.5a).

To further analyze the data, recourse to the theory outlined in Chapter 2 is necessary.

4.3. Data Analysis and Fitting Procedures

According to the development in Chapter 2, the experimentally observed signal, $S(t)$, should be a linear combination of the six calculated partial intensity patterns, $\Omega_{\ell|m_\ell|}(t)$ for the prevailing experimental conditions [Equations (21, 22)]. Figure 5 is a plot of these calculated partial intensities for the case when the observation axis is perpendicular to an applied electric field of 53 V/cm.

In order to facilitate the data analysis, a computer program to be used in conjunction with a remote graphic display terminal

(Tektronix Model T-4002) was developed. This routine allows the graphical display of the data and various manipulations of it. For instance, subroutines can add or subtract various sets of data, renormalize the data to any desired input, smooth the data, take Fourier transforms of the data, and least squares fit the data to various analytical expressions, or to the numerically evaluated calculation of the partial intensities. The results of all the operations on the data are stored in separate arrays and can, in turn, be treated as data for subsequent manipulations. All results can be graphically displayed, at will, in either a linear or logarithmic form. The fitting routine can fit an arbitrary function, depending upon up to eight parameters, to the data.

The least squares fitting method is based on the assumption that the optimum choice of fitting parameters is that set which minimizes the weighted sum of the squares of the deviation of the data, y_i, from the fitting function, $F(x_i, c_k)$. A measure of the goodness of fit can be defined as

$$\chi^2(c_k) = \sum_i \frac{1}{\sigma_i} (y_i - F(x_i))^2 , \tag{38}$$

where σ_i is the uncertainty in the ith data point, y_i. The best choice of the parameters, c_k, is that choice which minimizes $\chi^2(c_1, c_2, \ldots)$:

$$\frac{\partial \chi^2}{\partial c_k} = \frac{\partial}{\partial c_k} \sum_i \frac{1}{\sigma_i} (y_i - F(x_i))^2 = 0 . \qquad (39)$$

Assuming that a second order Taylor's series expansion in the fitting parameters, c_k, is sufficient to describe χ^2 near its minimum, Equation (39) results in the matrix equation (27):

$$\beta = \Delta c \cdot \alpha , \qquad (40)$$

where

$$\beta_k = - \frac{1}{2} \frac{\partial \chi^2}{\partial c_k} , \qquad (41)$$

and

$$\alpha_{jk} = \frac{1}{2} \frac{\partial^2 \chi^2}{\partial c_j \partial c_k} . \qquad (42)$$

By inversion of the curvature matrix, α, the change in the parameters, Δc_k, necessary to bring χ^2 to its minimum can be determined. A useful sidelight (38) is that the error matrix, $\epsilon = \alpha^{-1}$, determines the standard deviation of each of the calculated parameters.

In order to use this procedure to determine the optimum parameter values, it is necessary, first, to choose some starting values for the parameters, and, second, to iterate the solution until convergence is reached. This procedure is necessary because a second order Taylor's expansion of χ^2 will, in general, only be valid quite near

the minimum. The written routine determines α and β numerically by evaluating $\chi^2(c_1, c_2 \ldots)$ at neighboring values of the parameters. Thus, the routine is completely general and can be used with any fitting function. However, if the fitting function is a linear function of the parameters, the second order Taylor's expansion of χ^2 is completely valid and the best choice of parameters is found in a single iteration. This, fortunately, is the case when fitting to the partial intensities (Equation (21)).

From start to finish, the reduction of the data involves the following steps.

1) The data are entered into the computer.

2) Where appropriate, background scans are subtracted to give correct data.

3) A function of the form

$$f(x) = e^{-c_2 t}(c_1 + c_3 \cos[c_4(t-c_5)]) + c_6 \qquad (43)$$

is fitted to the data.

4) The calculated frequency, c_4, gives a value for the perturbed Lamb shift, which from Figure 3 determines the magnitude of the applied motional electric field. This value is checked against the measured field.

5) On the basis of the determined motional electric field, the partial intensities, $\Omega_{\ell|m_\ell|}(t)$ are calculated.

6) A preliminary curve fit to Equation (21) is attempted using the measured foil position as defining $t = 0$.

7) On the basis of this fit, small corrections for the foil position, and for the contribution of the hyperfine splittings to the decay rate of the $s_{\frac{1}{2}}$-$p_{\frac{1}{2}}$ beat, are estimated.

8) A final fit of the data to the adjusted partial intensities is made. An overall constant background is allowed as a fitting parameter in addition to the six relative cross sections, $\sigma_\ell |m_\ell|$.

9) An additional fit is made utilizing only the first 40 data points.

Because the calculations have not properly taken into account the effects of the hyperfine and Zeeman interactions, the results of steps 8 and 9, above, will differ. In fact it is usually found that the calculated individual cross sections within any ℓ-level, differ significantly according to how many data points are used in the calculation. However, the linear combinations, $\sigma_p = 2\sigma_{p1} + \sigma_{p0}$, and $\sigma_d = 2\sigma_{d2} + 2\sigma_{d1} + \sigma_{d0}$ are found to be relatively insensitive to the number of data points retained. This is reasonable since, for instance, $\Omega_{p0}(t)$ and $\Omega_{p1}(t)$ are very similar, as shown in Figure 5. Also, the significant difference between the two is a rather slow variation of their difference. The extent to which this variation can be compensated for, by the background parameter, will depend upon the number of data points.

Typical curve fitting results are shown in Figures 17, 18, 20 and 21. Values of the reduced χ^2_ν are, typically, five for Ly-β emission and two for Ly-α emission. The reduced χ^2_ν is defined as χ^2 divided by the number of degrees of freedom for the fit (38). Table I is a tabulation of some typical fitting results for various beam energies and field strengths used in the present experiment.

In order to test the predicted variation of beat amplitude with field strength (Figure 6), the following procedure for measuring beat amplitudes was used. First, the data are smoothed by taking three point averages of the data points, until the remaining amplitude of the $s_{\frac{1}{2}}$-$p_{\frac{1}{2}}$ beat is negligible. Then the actual data are normalized to the smoothed curve. The resulting "data" are roughly of the form of a sinusoidal oscillation about an average value of one. The amplitude of this oscillation is approximately the amplitude of the $s_{\frac{1}{2}}$-$p_{\frac{1}{2}}$ beat. The results of this procedure, for data taken at 250 keV, are shown as the data points in Figure 6. The large error bars indicated in Figure 6 reflect the fact that the smoothing process affects the data in other ways than just reducing the amplitude of the Lamb-shift beat. The results, however, are consistent with a cross section ratio $\sigma_s/\sigma_p = 1.75 \pm 0.25$.

Table I. Curvefitting results.[a]

Energy (keV)	Field (V/cm)	χ^2_ν	n	σ_s	σ_p	σ_{p1}/σ_{p0}	σ_d	σ_{d0}	σ_{d1}	Background
255	59.0	5.9	3	15957(95)	9999(80)	1.4[b]	8947(362)	-576(449)	1628(256)	-500(260)
305	40.5	5.7	3	4770(70)	4000(41)	1.4[b]	1727(272)	0[b]	87(240)	-134(23)
340	40.7	2.6	3	2413(30)	1760(19)	1.5[b]	710(60)	-40(39)	-28(48)	0[b]
340	63.7	2.8	3	2486(28)	1705(27)	1.5[b]	1241(114)	-68(120)	176(54)	-61(8)
405[c]	33.5	2.6	3	4875(74)	3610(38)	1.7[b]	1984(174)	1000(276)	0[b]	63(25)
405[d]	33.5	2.4	3	4894(75)	3580(39)	1.7[b]	1672(237)	723(305)	0[b]	112(38)
508	39.6	2.9	3	3985(50)	2818(36)	2.2[b]	1685(94)	0[b]	500[b]	-233(26)
508	52.9	4.7	3	4703(50)	3280(52)	2.2[b]	2249(200)	42(210)	468(94)	-313(26)
305	200	2.8	2	9153(163)	8638(88)	0.36(9)	---	---	---	296(20)
340	260	2.1	2	6679(124)	5060(98)	1.28(105)	---	---	---	294(23)

[a]Only the ratios of the "cross sections" determined for a given set of experimental conditions are physically significant. The absolute cross sections depend upon such experimental unknowns as detector efficiency and solid angle, precise beam current, etc.

[b]Held fixed during curvefitting.

[c]Fifty data points included in fit.

[d]First 40 data points only included in fit.

5. SOURCES OF ERROR

The final error associated with the measured cross section ratios is due to uncertainties in several experimental quantities. Since the cross section ratios are determined by a complicated numerical procedure, it is impossible to derive a simple relationship between the total errors in the cross section ratios and the errors in the experimental quantities upon which they depend. Therefore, the total assigned errors are estimated from heuristic considerations, and from the observed spread in the measured cross sections, rather than from a derived relationship. The separate sources of error, and their probable effect on the experiment, are discussed below.

5.1. Statistics and Fitting Uncertainties

Since the signal photons are detected randomly in time, within any sampling interval, the standard deviation associated with the total number of counts for that interval will be the square root of the number of counts. In the curve fitting program, the statistical uncertainties associated with the signal are taken into account. From these uncertainties, the program calculates a one standard deviation for each of the cross sections that it determines. Typically, these fitting uncertainties are ±2 percent for the σ_s/σ_p ratio.

5.2. Background

By definition, the background is that part of the recorded signal which does not correspond to Ly-α or Ly-β emission from the in-flight decay of beam atoms. Any signal pulses from the Channeltron multiplier which are not due to Ly-β (Ly-α) photons from the spontaneous decay of hydrogen atoms excited to the $n = 3$ ($n = 2$) state at the foil are, therefore, background.

The most likely sources of background are: 1) Ly-β (Ly-α) emission from hydrogen atoms which have cascaded from the $n = 4$ ($n = 3$) or higher states, 2) free electrons which strike the Channeltron causing erroneous pulses, 3) true background counts, i.e., those associated with cosmic rays and thermal effects in the detector, 4) x-rays formed by collisions of high energy electrons with metal surfaces visible to the detector, and 5) Ly-β (Ly-α) or similar wavelength emission from the excited background gas, or due to beam collisions with metal surfaces. True background (possibility #3) contributed negligibly in the present experiment (less than 5 counts/min.).

In order to study the other sources of background, a means of eliminating the true signal without disturbing the background is needed. By scanning the spectrometer across the spectrum from Ly-β (1026 Å) to Ly-α (1215 Å), those backgrounds which produce an

apparent wavelength continuum can be studied. It is observed that a continuum of, roughly, 5 percent of the Ly-β line does exist in some circumstances. This continuum is considerably reduced as the bias voltage on the Channeltron is increased. With a magnetic field present in the target region, this source is completely eliminated, except for a small region directly behind the foil. Evidently, the continuum is due primarily to high energy electrons, formed in the foil, which reach the detector surface. By maintaining a high negative bias voltage on the detector (-300 V), and by deleting the first two or three data points for analysis purposes, this source of background can usually be ignored. For those scans taken in low magnetic fields, a background scan was also taken at a wavelength of 1100 Å. This background scan can then be subtracted from the data to eliminate its effect (with the assumption that it is wavelength independent).

The possibility of a Ly-β (Ly-α) background, primarily due to cascades, still remains. A reasonable assumption is that this remaining background is constant over the observed region [certainly the lifetimes of higher lying levels are considerably longer than τ_{3p} (τ_{2p})]. The fitting routines used can allow for a constant background. The value determined for this background varies greatly from scan to scan but always accounts for less than 2 percent of the peak signal. If the background is arbitrarily set equal to zero, the fitting results are slightly less satisfactory (χ^2_ν is increased by one,

typically), and the cross sections determined differ by various amounts. The extent to which the fitting results differ, when the background parameter is alternately included and excluded, is a measure of the uncertainty introduced to the results by this background. Half of this difference is arbitrarily selected as the uncertainty due to background. Typically this factor is about 2 percent for the σ_s/σ_p ratio.

5.3. Hyperfine and Zeeman Effects

In Section 2.5b it was shown that the principle effects of the Zeeman and hyperfine interactions could be compensated for by an adjustment of the rate of decay associated with the $s_{\frac{1}{2}}$-$p_{\frac{1}{2}}$ beat. In an example based on calculations for a $j = \frac{1}{2}$ system, it was shown that after this adjustment the relative error remaining in the measured ratio σ_s/σ_p would be 1.5 percent. Although the effect on the ratio σ_d/σ_p is more difficult to establish, since no single beat amplitude determines this ratio, an absolute uncertainty of ±0.2 can be taken as an upper limit at the fields used in this experiment.

5.4. Slit Function

In the data analysis the effects of the slit function were included by an integration of the calculated intensity over the measured slit function. The uncertainty in the slit function itself will introduce an

error in the calculations. This effect is negligible compared with other sources of error in the present experiment.

5.5. Velocity and Field Uncertainties

As discussed in Section 3.2 the velocity of the beam is uncertain by about one percent due to uncertainties in the operating voltage of the accelerator and the stopping power of the foil. In the data analysis, the nominal particle velocity (calculated from the measured accelerator energy and the estimated foil loss) was assumed correct. For calculational purposes, the motional electric field present was taken as that value which gave the observed spatial periodicity of the $s_{\frac{1}{2}}$-$p_{\frac{1}{2}}$ beats in the intensity pattern.

An actual beam velocity one percent below the nominal value would produce an intensity pattern with spatial periodicity one percent higher than nominal. Consequently, at 40 V/cm, the erroneously high $s_{\frac{1}{2}}$-$p_{\frac{1}{2}}$ frequency would be compensated for by the choice of an applied electric field approximately 2 percent (Figure 3) greater than actually present. The observed $s_{\frac{1}{2}}$-$p_{\frac{1}{2}}$ beat amplitude would then imply a cross section ratio, σ_s/σ_p, (Figure 6), about 2 percent low. Other cross section ratios will be similarly affected. Therefore, velocity uncertainties attribute an uncertainty of about 2 percent to the calculated cross sections.

Another point to consider is the possible non-uniformity of the

magnetic field. This nonuniformity will produce beat frequencies which vary over the observed path. Therefore, beat amplitudes, and consequently cross section ratios, will be difficult to determine. In this work it was established that fields were uniform to ±1 percent over the region of observation. The effect of nonuniformities is at most, then, a frequency variation of about 1 percent over the observed region. Consequently, the largest phase shift, with respect to the pattern in a uniform field, would be about 30° for an observation extending over ten beats. The effect of an error of this type is more to increase the χ^2_ν of the fitting function, than to change any of the determined cross sections. Since, in the final analysis, only as many data points were included as could be fitted with reasonably small χ^2_ν, the effects of field nonuniformity are already included, indirectly, in the fitting uncertainties.

5.6. The Intrinsic Polarization of the Spectrometer

The spectrometer polarization factor, g, is uncertain by nearly 10 percent (see Appendix A). Fortunately, for a $j = \frac{1}{2}$ system, the emitted radiation is unpolarized (37). Since the σ_s/σ_p ratio is determined, principally, from the $s_{\frac{1}{2}}$-$p_{\frac{1}{2}}$ beat, the variation of g over its permissible range, in the calculation of the partial intensities, results in a variation of the $s_{\frac{1}{2}}$-$p_{\frac{1}{2}}$ beat by about 5 percent. This figure is taken as the uncertainty in the ratio σ_s/σ_p

due to the error in g. Note, however, that this error should effect all data approximately equally. Therefore, it has little or no effect on the relative variation of the cross sections with beam energy.

5.7. Summary

Adding together the various uncertainty contributions discussed above results in an overall uncertainty for the σ_s/σ_p ratio of approximately 12 percent. This estimation should be taken as a maximum possible error rather than a probable error since all uncertainties were awarded liberally. The ratio, σ_d/σ_p, is determined with less precision since its contribution to the signal is more subtle and since it is hard to distinguish between contributions from d-states and cascades or background contributions over the time scales typical here. The overall errors indicated in Table II are determined from these considerations and also by the self consistency of the data itself, e.g., the cross sections should be independent of the applied field.

6. DISCUSSION

The purpose of the present experiment is both to verify that the theory developed, together with the method of calculation, are an adequate description of an atom created suddenly in an applied electric field; and to use this theory to obtain information about the beam-foil interaction, in the form of relative cross sections for excitation of hydrogen in the different ℓ-orbitals within the $n = 3$ or $n = 2$ levels.

Once the experimental unknowns (the relative cross sections) for a given beam energy are established, the intensity pattern at other field strengths or field orientations can be calculated, since the theory assumes the excitation process is independent of the magnitude of the external field. Figure 6 compares the measured and calculated $s_{\frac{1}{2}}$-$p_{\frac{1}{2}}$ beat amplitudes for Ly-β emission as a function of the electric field strength. The results are consistant with a cross section ratio $\sigma_s/\sigma_p = 1.75 \pm .25$. These data were taken at 250 keV in motional fields perpendicular to the plane of observation. Data at other energies also indicate a dependence of the $s_{\frac{1}{2}}$-$p_{\frac{1}{2}}$ beat amplitude on field strength in essential agreement with theory. Figure 20 compares independent theoretical fits to data taken at different field strengths but in otherwise identical experimental conditions. The cross sections determined for these separate data are consistent to

within the experimental uncertainties, again confirming the theory.

A more rigorous test of the theory is its ability to predict the variation of the intensity pattern with field orientation relative to the plane of observation. This variation critically depends upon fundamental assumptions about the beam alignment (Section 2.2-2.4), since the field direction determines not only the extent of mixing, but also the actual states mixed by the Stark perturbation. Figure 18 is a comparison of Ly-β data taken with the motional electric fields parallel and perpendicular to the plane of observation. The field strength is 40 V/cm and the beam energy is 300 keV. Independent theoretical fits to the two patterns yield cross sections consistent to within the fitting uncertainties. Again the theory accounts for the observed effects. It is noteworthy that the $j = \frac{3}{2}$ beats are strongly enhanced when observed along the induced dipole.

In Section 2.5b it was shown that, for the observation times used in the present experiment, the Zeeman interaction should influence the data only to the extent of a slightly more rapid decay of the $s_{\frac{1}{2}}$-$p_{\frac{1}{2}}$ beat. Except for the effects of the fringing field, those data in electric and motional electric fields should therefore be nearly identical. Figure 19 is a comparison of Ly-β data taken in static and motional electric fields. The observed effect is approximately a 60° phase shift and a 25% beat attentuation of the electrostatic field beats relative to those in a motional field. This is in good agreement with the

expected fringing field effects (Figure 9) discussed in Section 2.5c. Similar comparisons for Ly-α data also agree with the predictions of Figure 9 to within an accuracy of about 10 percent.

The theory of quantum beats (Section 2.2b) is found to accurately describe the observed dependence of the intensity pattern on both field strength and direction. An extension of the calculations to include a nonuniform field is found to predict the intensity pattern in an electrostatic field where fringing effects must be considered. Our conclusion is that the theory of quantum beats, as developed in Chapter 2, is an adequate model of quantum beat phenomena. This theory depends upon both the assumptions of Macek (6) regarding the symmetry of the beam foil interaction, and the assumption that the Bethe-Lamb equations are an adequate description of the excited state. The discrepancies reported by Andrä (11), between data taken in static and motional electric fields, were not observed in the present experiment. These discrepancies may be due to the effects of the fringing field which were not considered in Andrä's experiment.

Table II summarizes the relative cross sections determined in the present experiment. The errors indicate the absolute uncertainties, due to both experimental inaccuracies and the approximations made in the calculations, as discussed in Chapter 5.

Also listed in Table II are results of other experimenters. Although the present work is in good agreement with values obtained

Table II. Measured cross section ratios for beam-foil formation of atomic hydrogen in n = 2 and n = 3 levels.

Energy (keV)	Source	σ_s/σ_p	σ_d/σ_p	σ_{d2}/σ_d
	Statistical Expectation	1/3	5/3	1/5
n = 2				
150	Sellin (10)[a]	<1/3	---	---
200	Andra (11)[a]	0.08 (2)	---	---
233	Bickel (9)[b]	1.45 (20)	---	---
305	present study[a]	1.10 (10)	---	---
340	present study[a]	1.32 (10)	---	---
n = 3				
~100	Bukow (12)[c]	1.64 (8)	0.69 (4)	---
255	present study[a]	1.65 (15)	0.70 (20)	$\geq$ 0.3
305	present study[a]	1.30 (20)	0.45 (15)	---
340	present study[a]	1.42 (10)	0.59 (18)	$\geq$ 0.3
405	present study[a]	1.45 (10)	0.50 (15)	$\geq$ 0.3
508	present study[a]	1.42 (10)	0.65 (15)	$\geq$ 0.3

[a] Quantum beats method.

[b] Stark modified mean lifetime of the n = 2 levels.

[c] Mean decay rate for H_α radiation in zero field.

from mean lifetime measurements (9, 12), the previous quantum beat experiments for $n = 2$ are in serious disagreement. Although a large variation in the relative cross sections with beam energy could account for all the results reported for $n = 2$, this seems unlikely since the $n = 3$ cross section ratios are observed to be relatively constant with beam energy (Table II).

The observation of a beat maximum at the foil would appear to be conclusive proof of preferential initial population of the $p_{\frac{1}{2}}$-levels relative to the $s_{\frac{1}{2}}$-levels ($\sigma_p > 3\sigma_s$). In Sellin's experiment (10), however, a slit function wide enough to result in an apparent phase shift of the beat by nearly half a wavelength leaves the conclusions somewhat open to speculation. It should be pointed out that considerable care was exercised in the present experiment to establish the absolute position of the foil and the effect of the slit function on the intensity pattern.

Although Sellin (10) employed a motional electric field, Andrä (11), for the most part, used an electrostatic field parallel to the beam axis by utilizing the foil holder as one field plate. As discussed in Section 2.5a, initial coherence between the s- and p-levels can influence the signal in this case, although Andrä could adequately interpret his parallel field data without including this possibility. Resolution of the apparently contradictary results for $n = 2$ should provide a worthwhile subject for some future investigation, but is

beyond the scope of the present experiment.

Relative excitation cross sections for the ℓ-states within the $n = 3$ and $n = 2$ levels have been established, in the present investigation, at several beam energies (Table II). These values, together with previous measurements of the initial m_ℓ alignment (8, 16, 20), should provide a useful test for any proposed theory of the excitation process.

BIBLIOGRAPHY

1. Bethe, H. and E. Salpeter. Quantum mechanics of one- and two-electron atoms. New York, Academic Press, 1957. 368 p.

2. Bashkin, S. ed. Beam foil spectroscopy. New York, Gordon and Breach, 1968, 180 p.

3. Garcia, J.D. Foil excitation mechanisms. Nuclear Instruments and Methods 90:295-298. 1970.

4. Bickel, W.S. et al. Multi-collisional molecular orbital model for the beam-foil interaction process. Nuclear Instruments and Methods 90:309-314. 1970.

5. Hughes, R.H., H. Dawson, and B. Doughty. Measurement of the lifetimes of the n = 3 states of H by electron capture during H^+ impact on gases. Journal of the Optical Society of America 56:830-831. June, 1966.

6. Macek, J. Theory of atomic lifetime measurements. Physical Review A 1:618-627. March, 1970.

7. Macek, J. Interference between coherent emissions in the measurement of atomic lifetimes. Physical Review Letters 23:1-2 July 7, 1969.

8. Lynch, D.J. Observation of fine structure interference effects in Lyman-beta radiation from beam-foil excited hydrogen atoms. Doctoral dissertation, Oregon State University, 1972. 72 numb. leaves.

9. Bickel, W.S. Electric-field and multiple-foil excitation experiments on beam-foil excited hydrogen atoms. Journal of the Optical Society of America 58:213-221. February, 1968.

10. Sellin, I.A. et al. Periodic intensity fluctuations of Balmer lines from single foil excited fast hydrogen atoms. Physical Review 188:217-221. December 1969.

11. Andrä, H.J. Stark-induced quantum beats in H Ly-alpha emission. Physical Review A 2:2200-2207. December, 1970.

12. Bukow, H. et al. Lifetimes and initial populations of foil-excited hydrogen and lithium states. Nuclear Instruments and Methods, to be published.

13. Sellin, I.A. et al. Periodic intensity fluctuations of Balmer lines from single foil excited fast hydrogen atoms. Physical Review 184:53-63. August, 1969.

14. Andrä, H.J. Quantum beats and level crossing after beam foil excitation. Nuclear Instruments and Methods 90:343-349. August, 1970.

15. Percival, I.C. and M.J. Seaton. The polarization of atomic line radiation excited by electron impact. Philosophical Transcripts of the Royal Society A 251:114-138. November, 1958.

16. Lynch, D.J. et al. Zero field quantum beats in Lyman-β radiation from beam-foil-excited hydrogen atoms. Physical Review Letters 26:1211-2131. May, 1971.

17. Andrä, H.J. Zero-field quantum beats subsequent to beam-foil excitation. Physical Review Letters 25:325-327. August, 1970.

18. Burns, D. and W. Hancock. Zero-field intensity oscillations following impulsive excitation of hydrogen. Physical Review Letters 27:370-372. August, 1971.

19. Berry, H.G. and J. Subtil. Fine-structure measurements by the beam-foil technique. Physical Review Letters 27:1103-1104. October, 1971.

20. Dobberstein, P., H.J. Andrä, and W. Wittman. Zero-field quantum beats in Lyman-alpha radiation subsequent to beam-foil interaction of protons. Zeitschrift für Physik 257:272-278. December, 1972.

21. Lamb, W.E., Jr. Fine structure of the hydrogen atom. Part III. Physical Review 85:259-276. January, 1952.

22. Johnson, C.E. A comment on the Lamb-shift measurements using electric field quenching. Bulletin of the American Physical Society 17:454. April, 1972.

23. Holt, H. and I. Sellin. Time-dependent theory of Stark quenching of 25 states in hydrogen and helium. Physical Review A 6:508-510. July, 1972.

24. Fontana, P.R. and D.J. Lynch. Radiative decay of coupled atomic states. Physical Review A 2:347-352. August, 1970.

25. Grisaru, M., H. Pendleton, and R. Petrasso. On the Bethe-Lamb equations. Submitted to The Annals of Physics, 1973.

26. Merzbacher, E. Quantum Mechanics. New York, John Wiley and Sons, 1961. 544 p.

27. Ehrlich, L. Eigenvalues and eigenvectors of complex non-hermitian matricies using the direct and inverse power methods and matrix deflation-computer program. University of Texas. August, 1961.

28. Wangsness, R. Stark-induced temporal intensity vibrations in spectral lines. Physical Review 149:60-61. September, 1966.

29. Series, G.W. Proposal for measuring Lamb shifts by the study of modulated, fluorescent light. Physical Review A136:684-688. November, 1964.

30. Lefevre, H. and C. Burke. Calibration curve for generating voltmeter - U. of Oregon Accelerator log book. Eugene, Oregon, 1970.

31. Graves, P.W. et al. Operation of Channeltron and Spiraltron electron multipliers in the pulse saturated mode. Bendix Research Corporation Technical Applications Note 6902: Ann Arbor, Michigan. May, 1969. 14 p.

32. Ramsey, N. Molecular beams. London, Oxford University Press, 1963. 453 p.

33. Sampson, J. Techniques of ultraviolet spectroscopy. New York, John Wiley and Sons, 1967. 348 p.

34. Schmidt, K. and C. Hendee. Continuous channel electron multiplier operated in the pulse saturated mode. I.E.E.E. Transactions on Nuclear Science 13:100-111. June, 1966.

35. Johnson, M. and J. Svenson. Absolute quantum efficiency of a channeltron photomultiplier. Bendix Research Corporation Technical Note: Ann Arbor Michigan. December, 1966. 6 p.

36. Northcliffe, L. Passage of heavy ions through matter. Annual Review of Nuclear Sicnece 13:67-102. 1963.

37. Wooten, J.W. and J.H. Macek. Polarization of quench-induced Ly-α radiation. Physical Review A 5:137-140. January, 1972.

38. Bevington, P.R. Data reduction and error analysis for the physical sciences. New York, McGraw-Hill Book Company, 1969. 336 p.

39. Rabinovitch, K. et al. A method for measuring polarization in the vacuum ultraviolet. Applied Optics 4:1005-1010. August, 1965.

40. Carver, T.R. and R.B. Partridge. Monitoring operators in magnetic resonance and light modulation. American Journal of Physics 34:339-350. 1966.

APPENDICES

APPENDIX A

Measurement of the Intrinsic Polarization of the Spectrometer

The theory involved in the determination of the spectrometer polarization parameter, g, is developed in reference (39) and in an appendix to reference (8). The basic result of that discussion is

$$g = \frac{R_2\sqrt{1+4(R_1+R_2)} - R_2 + 2R_1}{R_1\sqrt{1+4(R_1+R_2)} - R_1 + 2R_2} , \qquad (37)$$

where polarization parameter, g, is defined as the ratio of detection efficiencies for light polarized parallel and perpendicular to the spectrometer slits. The quantities R_1 and R_2 are the measured reflectances from an opaque, homogeneous, non-magnetic material oriented such that the plane of incidence of the light is perpendicular and parallel, respectively, to the exit slit of the spectrometer.

Figure 22 shows the experimental arrangement used to measure R_1 and R_2. The spectrometer was tuned to pass Ly-β radiation, from an unpolarized light source, through the exit slits of the spectrometer. A pinhole insert at the exit slits served to define a pencil beam of light. The reflecting surface and detector "A" could be rotated in unison about the beam axis. The ratio of photon count rates with the plane of incidence horizontal and vertical is the ratio R_1/R_2. The absolute reflectance, R_1, was also determined by

measuring the count rate on Detector "B" when the reflecting surface was moved to one side. To allow for the possible different quantum efficiencies of the two detectors, they were exchanged and the measurement repeated.

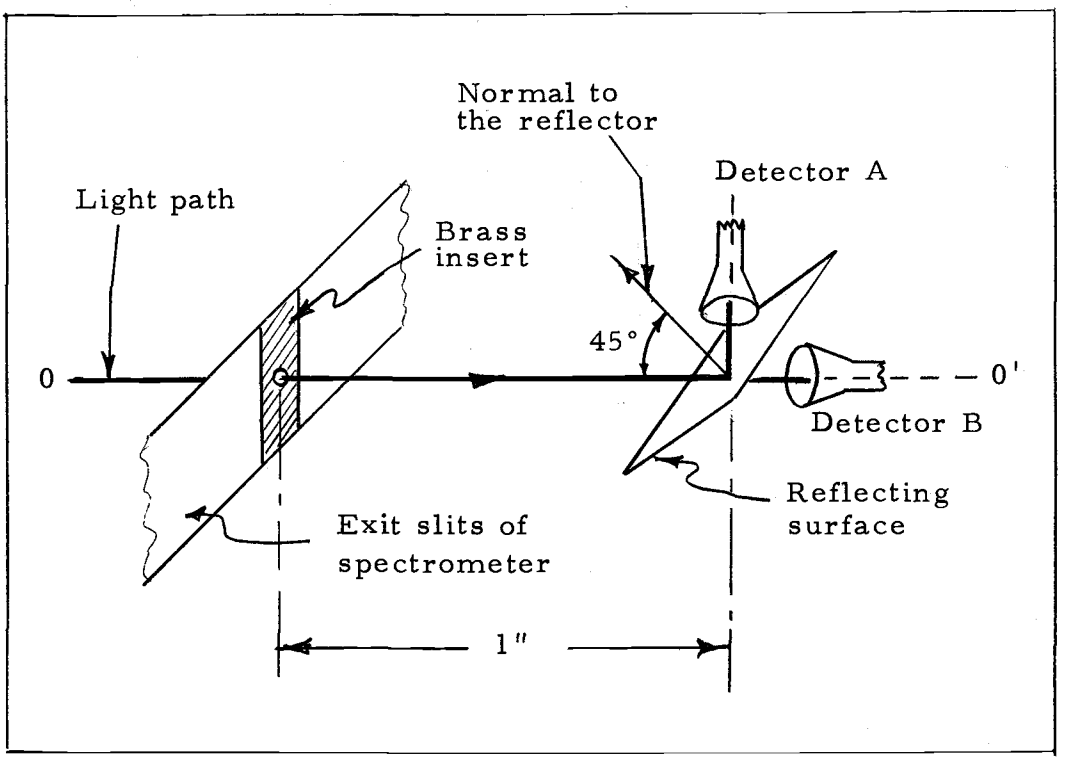

Figure 22. The experimental setup used in measuring R_1 and R_2. Detector A and the reflecting mirror can rotate as a unit about the axis 0-0' to measure the ratio R_1/R_2. The reflecting surface can also be removed from the light path so that the absolute value of R_2 can be determined by comparing count rates in A and B.

Both quartz and ordinary microscope slide glass were used as the reflecting surface. The results are indicated in Table A. 1.

The final value is taken as $g = 3.4 \pm .3$. A sidelight of this measurement is that it was experimentally determined (by recording

count rate vs angle of the plane of incidence from the horizontal) that the major optical axis of the detection system is parallel to the spectrometer entrance slits.

Table A-1. Summary of intrinsic polarization measurements.

Reflector	R_1	R_2	g
Quartz	0.201 (7)	0.104 (6)	3.20 (25)
Glass	0.183 (8)	0.085 (6)	3.60 (25)

APPENDIX B

Measurement of the Slit Function

In order to properly take into account the effect of the finite field of view of the spectrometer on the observed signals, it is necessary to know the slit function $f(t, t')$ which is defined in Section 2.3. This appendix describes the determination of the slit function corresponding to the configuration of the signal detection system used in part of the present experiment.

The apparatus used to determine the slit function is shown schematically in Figure 23. The point on the beam axis at the center of the field of view of the spectrometer is defined to be z. All points z' on the beam axis for which $|z-z'| < \delta$ are "seen" by all points of the grating and therefore contribute equally to the integrated signal. Points z' in the range $\delta \leq |z-z'| \leq \epsilon$ are visible to only a fraction of the total grating surface, and therefore contribute to the total signal proportionately.

The slit function was experimentally determined by the following method. A helium-neon laser was mounted on a linear micrometer drive which translated parallel to the line representing the beam axis, with the laser axis perpendicular to the beam axis as shown in Figure 23. A lens focused the laser light on the beam axis line. The focused laser light completely filled the entrance slit of the spectrometer when

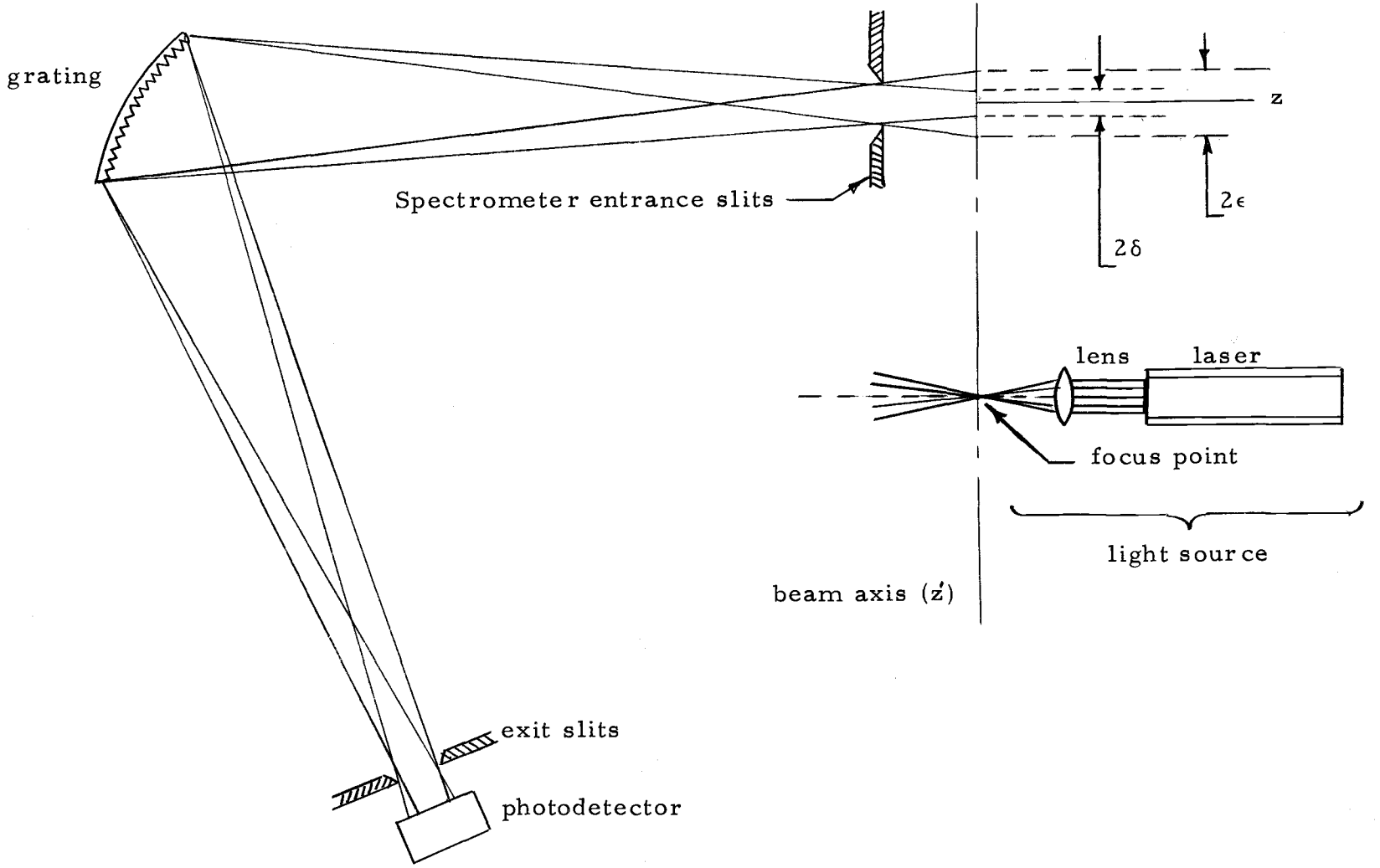

Figure 23. The arrangement used to determine the slit function of the spectrometer. The laser assembly translates parallel to the beam axis.

the focus point was at z on the beam axis. The focus point thus represented a point light source on the beam axis as seen by a detector at the exit slit of the spectrometer. The slit function was therefore measured directly by plotting the signal from the calibrated light detector versus the position, z', of the focus point along the line representing the beam axis. This curve is shown in Figure 24. The detector was a vacuum photodiode (R. C. A. model 922). It was calibrated to determine that the voltage output varied linearly with incident intensity on the photocathode.

It should be noted that this entire development assumes that the slit function is independent of wavelength since the results of a measurement in the visible region of the spectrum are applied to data reduction of intensity measurements in the extreme ultraviolet range. The slit function was also calculated (32) from the known spectrometer parameters to verify the experimental results given in Figure 24.

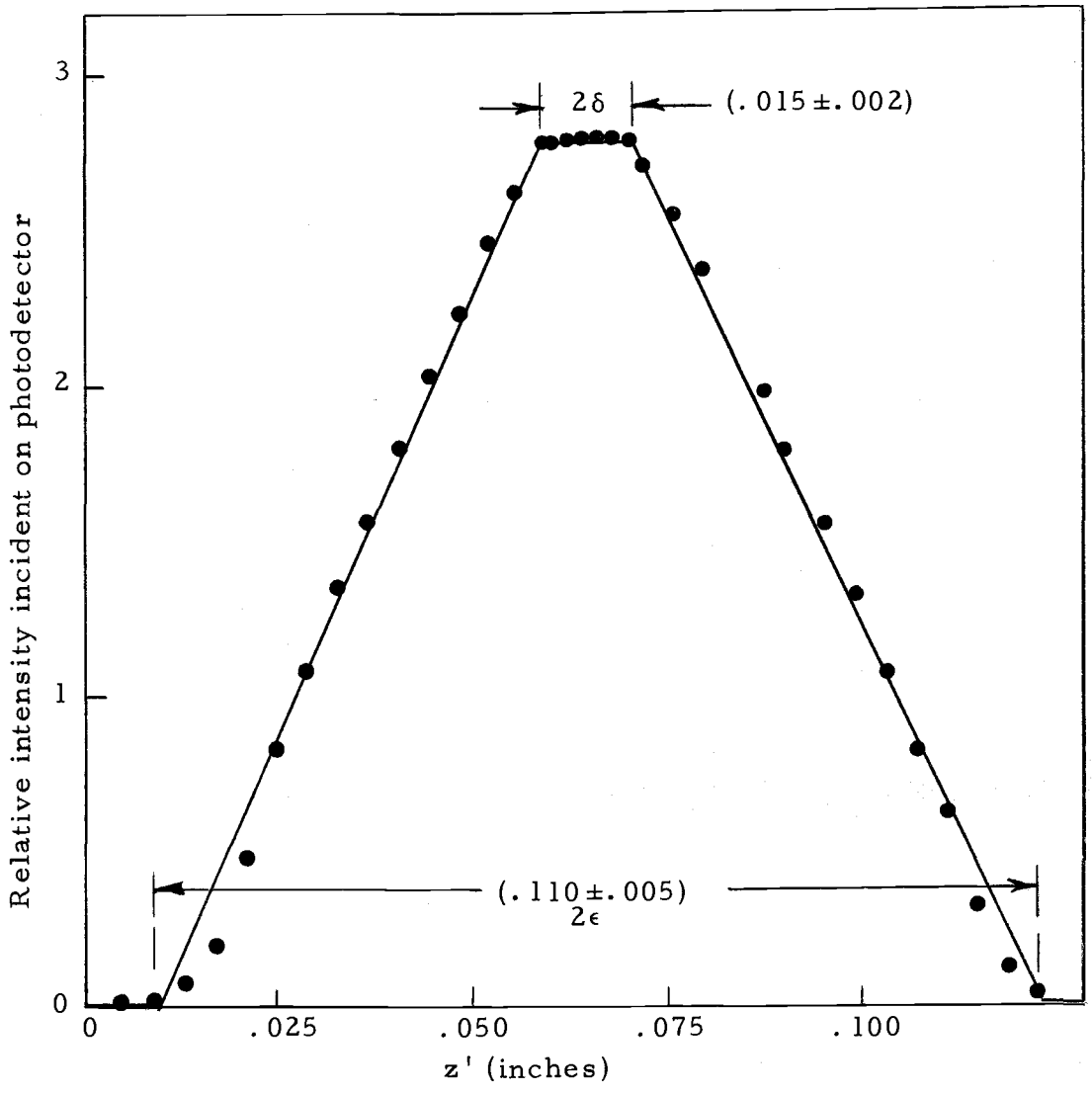

Figure 24. The intensity at the photodetector vs the relative position of the light source along the beam axis.

APPENDIX C

Measurement of the Absolute Position of the Foil Corresponding to $t = 0$

In a separate experiment the absolute position of the carbon foil target corresponding to $t = 0$ for the beam-foil excitation was determined. In this experiment, the detector at the exit slit of the spectrometer in Figure 23 was replaced by the laser-lens system described in Appendix B, such that the focus point of the laser light was at the exit slit and the light from this source completely filled the grating surface. The grating was set for zero-order reflection so that light reflected from the grating passed through the entrance slit of the spectrometer and was incident on the line representing the beam axis in Figure 23. The position which corresponds to $t = 0$, was then determined by visually centering the back edge of a foil holder on the illuminated section of the beam axis line. This was accomplished by visually determining the end points of the illuminated section in repeated measurements. The point corresponding to $t = 0$ was determined to be $8.266 \pm .010$ inches on the micrometer dial which drives the target wheel along the beam axis.

It is also possible to determine the $t = 0$ position from the signal decay itself. When the spectrometer field of view is exactly centered about the foil, only half of the grating sees the beam and the

intensity is half that measured when the entire field of view is downstream from the foil. Thus, as the foil is scanned past the spectrometer the signal should rise sharply, reaching half its maximum at a position roughly corresponding to the absolute position $z = 0$.

If the slit function is asymmetric, or if the light intensity itself varies appreciably over the distance of one slit width, or if a large background is present in this region, the determination of $z = 0$ by this method will be in error. The symmetry of the slit function is demonstrated in the preceding section. It was an observed fact that intensities did not vary significantly over the slit width. Background, however, was frequently large near the foil for low magnetic fields. A foil holder which collimated the beam to 1/8" diameter was found to eliminate most of the background problems.

A third method for determining the foil position was a visual alignment of the back edge of the foil holder with the center of the spectrometer slits. This alignment was limited in precision by the difficult angle of view allowed by the viewing ports in the target chamber. Nevertheless, repeatability of ±0.020 inches could be obtained. This method provided a quick check of the alignment for each run and also was suitably precise for most of the data.